

Caenorhabditis elegans screen reveals role of PAR-5 in RAB-11-recycling endosome positioning and apicobasal cell polarity

Julia Franziska Winter^{1,3}, Sebastian Höpfner^{1,3,4}, Kerstin Korn^{2,4}, Benjamin O. Farnung^{1,4}, Charles R. Bradshaw^{1,4}, Giovanni Marsico¹, Michael Volkmer^{1,4}, Bianca Habermann^{1,4} and Marino Zerial^{1,5}

Apically enriched Rab11-positive recycling endosomes (Rab11-REs) are important for establishing and maintaining epithelial polarity. Yet, little is known about the molecules controlling trafficking of Rab11-REs in an epithelium *in vivo*. Here, we report a genome-wide, image-based RNA interference screen for regulators of Rab11-RE positioning and transport of an apical membrane protein (PEPT-1) in *C. elegans* intestine. Among the 356 screen hits was the 14-3-3 and partitioning defective protein PAR-5, which we found to be specifically required for Rab11-RE positioning and apicobasal polarity maintenance. Depletion of PAR-5 induced abnormal clustering of Rab11-REs to ectopic sites at the basolateral cortex containing F-actin and other apical domain components. This phenotype required key regulators of F-actin dynamics and polarity, such as Rho GTPases (RHO-1 and the Rac1 orthologue CED-10) and apical PAR proteins. Our data suggest that PAR-5 acts as a regulatory hub for a polarity-maintaining network required for apicobasal asymmetry of F-actin and proper Rab11-RE positioning.

The polarity of simple columnar epithelial cells, such as those lining the luminal surface of the intestine, is characterized by three main inter-dependent hallmarks: (1) apicobasally organized cytoskeletal components¹ and polarity regulators²; (2) two compositionally and functionally distinct apical and basolateral plasma membrane surfaces separated by intercellular junctions³; (3) a sophisticated network of membrane organelles, some of which are asymmetrically distributed, such as apical Rab11-positive recycling endosomes (Rab11-REs; ref. 4). The epithelial membrane trafficking system is both complex and robust owing to multiple sorting mechanisms and parallel transport routes to ensure the delivery of cargo to its correct destination^{5,6}. Elucidating the regulatory networks that couple the organization of the membrane traffic system to establishment and maintenance of epithelial polarity remains an ongoing quest. In this respect, particular attention has been given to a set of evolutionarily conserved master regulators including PAR proteins and small GTPases of the Rho and Rab families⁷.

The PAR family comprises seven functionally diverse proteins originally described in the roundworm *Caenorhabditis elegans*⁸. The apical PAR proteins PAR3, PAR6, aPKC and PAR1 play specific roles in

epithelial polarity, such as cytoskeletal organization^{9,10}, apical junction formation¹¹ and maintenance¹², and basal membrane positioning¹³. Rho GTPases (ref. 14) such as RhoA, Cdc42 and Rac1 co-ordinately regulate actin polymerization, actomyosin contractility or both through both distinct and shared effector proteins². PAR proteins are both effectors and regulators of Rho GTPases, modulating their activity and crosstalk, as well as the localization of other cytoskeletal regulators and components². Rab GTPases are key determinants of functional identity of membrane organelles^{15,16}.

Among the membrane organelles, Rab11-REs play a prominent role both in establishing and maintaining epithelial polarity^{17,18}. Rab11-REs mediate recycling and sorting of both apically^{19,20} and basolaterally²¹ endocytosed membrane components, and can function as secretory transport intermediates between the Golgi complex and plasma membrane²². Notably, Rab11-REs enrich apically in polarized epithelia across metazoans^{4,23}, including the intestine of *C. elegans* (ref. 24, this study). The *C. elegans* intestine has become an attractive organ model system for studying epithelial polarity^{11,25}, trafficking²⁶ and cytoskeletal regulation^{27,28}. It comprises 20 enterocytes that line up bilaterally with two or four cells per segment²⁹.

¹Max Planck Institute of Molecular Cell Biology and Genetics, MPI-CBG, Pfotenhauerstrasse 108, 01307 Dresden, Germany. ²High-Throughput Technology Development Studio, MPI-CBG, 01307 Dresden, Germany. ³These authors contributed equally to this work. ⁴Present addresses: Bird & Bird LLP, Pacellistrasse 14, 80333 Munich, Germany (S.H.); Cenix BioScience GmbH, Tatzberg 47, 01307 Dresden, Germany (K.K.); ETH Zürich, Institut für Biochemie, HPM E 17.1, Schafmattstrasse 18, 8093 Zürich, Switzerland (B.O.F.); Wellcome Trust and Cancer Research UK Gurdon Institute, University of Cambridge, Cambridge CB2 1QN, UK (C.R.B.); Max Planck Institute for Biology of Aging, Robert-Koch-Strasse 21, 50931 Cologne, Germany (B.H.).

⁵Correspondence should be addressed to M.Z. (e-mail: zerial@mpi-cbg.de)

In this study, we aimed to gain insights into the coordination between epithelial membrane traffic, cytoskeleton and polarity machineries *in vivo*. In particular, we were interested in identifying regulators of Rab11-REs and of the trafficking routes sustaining apical membrane transport. To achieve this in a systematic and unbiased manner, we carried out a genome-wide RNA interference (RNAi) screen in the *C. elegans* intestine.

RESULTS

Primary RNAi high-content screen

To establish a high-content, image-based assay, we generated a double transgenic screening strain (MZE1) that enabled monitoring of the intensity, subcellular position and morphology of three intestine-specific fluorescent markers (Fig. 1a): (1) green fluorescent protein (GFP) fusion to the Rab11a orthologue, RAB-11.1 (henceforth RAB-11), which labels apically-enriched Rab11-REs, (2) DsRed fusion to the apical membrane protein PEPT-1, a conserved H(+)-coupled oligopeptide transporter³⁰, and (3) autofluorescent lysosome related organelles (LROs; ref. 26), as indicators of general versus recycling-endosome-specific effects on organelle positioning and integrity. RNAi-treated worms were imaged by automated epifluorescence microscopy.

In pilot experiments, we verified that the distribution of PEPT-1::DsRed and GFP::RAB-11 change in a predictable fashion on RNAi of established transport regulators. We confirmed that PEPT-1 is suitable for reporting perturbations of apical membrane transport, and that GFP::RAB-11 recycling endosomes in *C. elegans* enterocytes share properties with Rab11-REs studied in mammalian and *Drosophila* epithelia^{23,31}, as they are distinct from Golgi and early endosomes (Supplementary Fig. S1g–l), traversed by apical membrane proteins (Fig. 1a and Supplementary Figs S1c,d, S5a,d), and their apical enrichment³¹ changes on depletion of RAB-11 effectors such as SEC-15 (ref. 23; Supplementary Fig. S1e,f). For the genome-wide RNAi analysis, we developed a semi-automated workflow (Fig. 1b) that uses the Ahringer RNAi feeding library³², whose 16,757 bacterial clones cover 87% of the *C. elegans* protein-coding genome. Each gene was analysed in at least two independent runs. The primary RNAi high-content screen (HCS) was split into two steps (primary screen methods are described in Supplementary Text S1). First, in the *emb* screen, we screened 1,037 *embryonic lethal* (*emb*) genes (~65% of genes essential for embryonic development and viability; WormBase release WS172) in the young-adult stage of the first generation. We validated the *emb*-screen images manually for altered phenotypes in marker distributions and intensities. Second, in the genome-wide screen (GWS), we screened the complete library in the young-adult stage of the second generation owing to increased RNAi phenotype frequency (percentage of worms with phenotypes) and increased strength (phenotype intensity in individual worms). To efficiently and objectively score RNAi phenotypes in the ~2.3 million images of the GWS, we developed an image analysis software and trained it on the *emb* screen images. This custom-built software is based on a noise-tolerant medial axis transform³³, enabling the analysis of multiple biometric parameters, for example worm shape, size (length, width, area), marker intensity, subcellular distributions and organelle morphology (Fig. 1d–g and Supplementary Fig. S2c).

In total, 356 candidate genes (*emb* screen, 209; GWS, 147; Supplementary Table S1) of sequence-authenticated feeding clones

were reproducibly identified. Overall, 88% of the 356 genes have orthologues in higher metazoans (82% in human, 3% in fly and 3% in mouse), underscoring the conservation of the epithelial membrane trafficking and polarity machineries.

Phenotypic profiles for functional inference

To classify alterations in intensity, position and morphology of the three fluorescent markers, we defined 14 phenotypic defect categories (Fig. 2a and Supplementary Fig. S2a and Table S1). To each gene we assigned a phenotype profile consisting of scores between 0 (wild type) and 3 (strong phenotypic defect) for each category. Genes sharing similar functions, such as those encoding subunits of multiprotein complexes (for example endosomal sorting complex required for transport (ESCRT), vacuolar H⁺-ATPases (V-H⁺-ATPases)), yielded similar phenotype profiles (Supplementary Table S2).

In the hit set, ‘membrane trafficking’ genes constituted the most abundant group (Fig. 2b and Supplementary Fig. S2b and Table S1) and ‘intracellular protein trafficking’ was the most enriched term (Protein Analysis Through Evolutionary Relationships (PANTHER) ontology³⁴, Fig. 2c), confirming that the screen indeed identified the genes it was designed for.

We next carried out hierarchical clustering³⁵ on all 356 phenotypic profiles (Supplementary Fig. S3e), capitalizing on the guilt-by-association principle³⁶. Within clusters, functionally known genes can be used to infer functional predictions for as-yet uncharacterized genes and genes previously not linked to epithelial polarity or membrane trafficking (illustrated with the compact clustering dendrogram in Supplementary Fig. S3a–d). Examples of functionally known and unknown candidates where we assigned functional roles are presented below and in Supplementary Table S3.

Comparative secondary assay analysis

For further comparative and functional analysis in secondary assays, we selected 60 genes mainly with phenotypic defects in GFP::RAB-11 positioning, PEPT-1::DsRed trafficking, or both, with known or unknown functions (Supplementary Table S3). The RNAi phenotype of each candidate was examined in transgenic worm strains expressing the apical membrane cargo PEPT-1::DsRed in combination with GFP-tagged markers for specific organelles, such as GFP::RAB-5 (early endosomes) or LMP-1::GFP (late endosomes) (Fig. 3b–f).

Among the 60 genes, 38 served as ‘reference candidates’, whose functions in membrane trafficking were mainly inferred from their orthologues, and on the basis of these we defined six phenotypically and functionally distinct ‘secondary assay’ groups (Supplementary Table S3 and Fig. 3a). For several secretory regulators and for components of the dynein and dynactin, ESCRT I and III and exocyst complexes we provided evidence for their role in membrane trafficking, organelle positioning or both in *C. elegans* enterocytes. The remaining 22 ‘test candidates’ comprised both functionally known and unknown genes and were assigned to the six secondary assay groups (Supplementary Table S3 and Fig. 3a). This confirmed numerous functional predictions inferred from the hierarchical clustering (Supplementary Fig. S3a,c). To gain mechanistic insights into RAB-11-RE positioning and function, we focused on candidates with either a general effect on endosome positioning or a more specific effect on RAB-11-REs (Supplementary Table S3, groups 5 and 6).

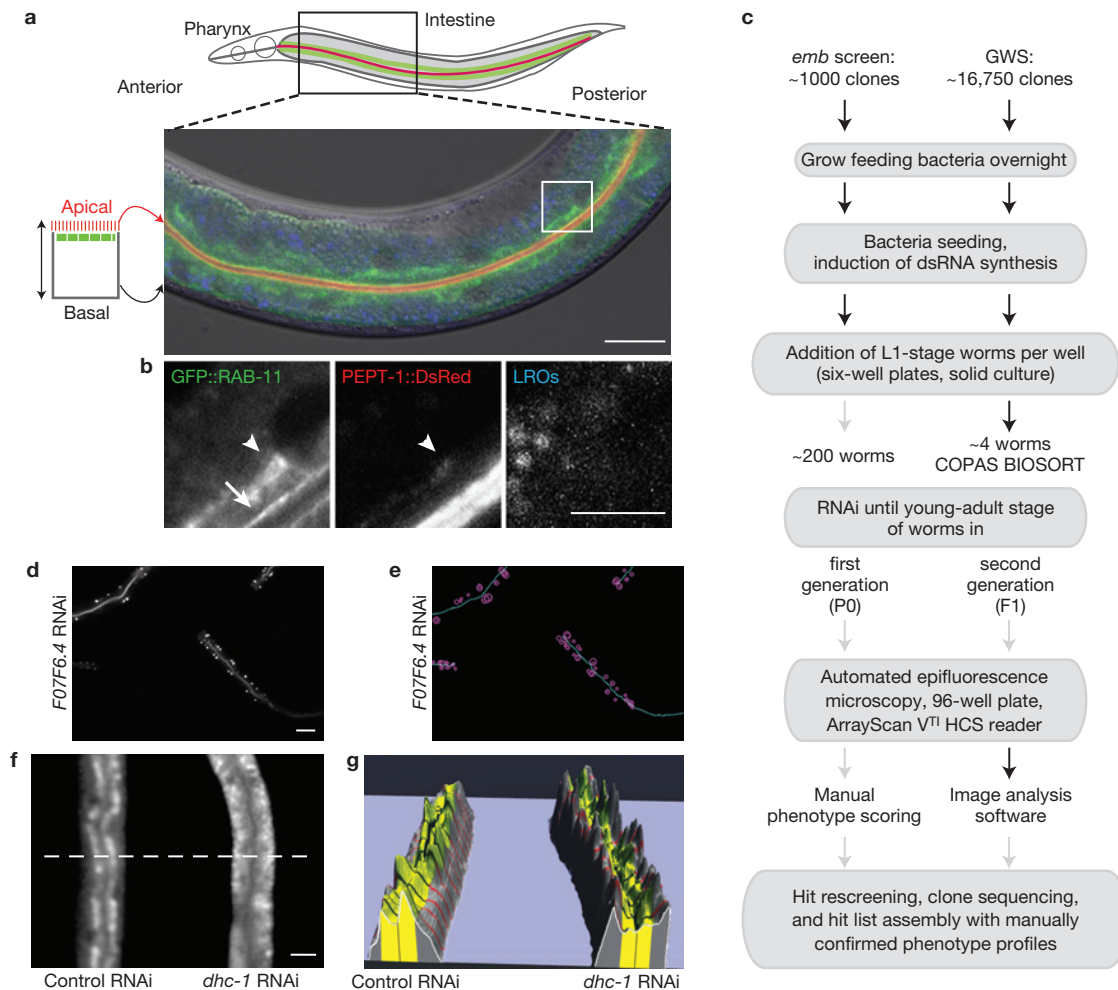


Figure 1 *In vivo* readout assay, semi-automated workflow and image analysis of the primary high-content screen. (a) Schematic depiction of the double transgenic nematode strain MZE1, and confocal and differential interference contrast microscopy images of the anterior intestinal region of an L4-stage animal. (b) Enlarged images corresponding to the boxed area in (a) showing the three markers. Small GFP::RAB-11-labelled recycling endosomes (arrow) align along the PEPT-1::DsRed-labelled apical membrane. Larger recycling endosomes (LROs; arrowhead) that can contain small amounts of PEPT-1::DsRed (arrowhead, brightness of enlarged image increased) concentrate subapically. Autofluorescent LROs in blue. (c) Scheme for

the semi-automated workflow of the primary screen. Black arrows indicate robotic steps, grey arrows manual steps. (d–g) Morphometric parameters determined by the custom-built image analysis include identification of the worm midline (d,e, cyan), intracellular punctate intensity maxima of PEPT-1::DsRed (d,e, magenta circles), RNAi of the *C. elegans* ARFGAP3 orthologue and detection of subcellular recycling endosome positioning (f,g). (g) Different intensity profiles of GFP::RAB-11 along apicobasal and medial axes of the intestines shown in (f) with REs enriched in the apical domain (yellow) in control RNAi (left) or in the basal domain (grey) on *dhc-1* RNAi (right). Scale bars, 10 μ m in (b) and 20 μ m in (a,d and f).

Microtubule-based recycling-endosome-positioning factors

Strikingly, all known candidates required for apical RAB-11-RE positioning were functionally associated with the microtubule cytoskeleton, including cytoplasmic dynein and dynactin complexes, the kinesin-1 orthologue UNC-116 and dynein-associated factors³⁷ such as LIS-1, NUD-1 and NUD-2, as well as F55C12.1, the orthologue of the Rab11 effector NUF (ref. 38, Supplementary Table S3, group 5, and Fig. 3a,d). This group included as-yet uncharacterized genes, such as C32D5.11, a predicted E3 ubiquitin ligase, which may regulate motor or cytoskeleton components. RNAi of these components caused similar phenotypes on all endosomal compartments tested, including the scattering or basal accumulation of recycling endosomes, late endosomes (Fig. 3d) and early endosomes (not shown). Furthermore, whereas only 20% of intestines treated with control RNAi ($n = 54$) had PEPT-1::DsRed present in GFP::RAB-11-REs, over 50% of

intestines treated with *arp-1*, *dhc-1* or *nud-1* RNAi ($n = 30$) exhibited increased amounts of PEPT-1::DsRed in scattered and basally misplaced GFP::RAB-11-REs (data not shown).

UNC-116 (kinesin-1 heavy chain) was the only identified microtubule plus-end kinesin. Its depletion similarly altered the apical distribution of both recycling endosomes and late endosomes (Fig. 3d), suggesting that kinesin-1 transports different endosomes in *C. elegans* enterocytes. It may also be required for dynein-mediated transport, as shown in *C. elegans* neurons³⁹. However, the complementing phenotypes observed on depletion of dynein and dynactin components versus UNC-116 (kinesin-1) rather suggest that apical enrichment of RAB-11-REs in *C. elegans* enterocytes requires coordinated minus- and plus-end microtubule-based transport.

Overall, our results highlight the importance of the dynein–dynactin machinery and identify further components for (1) minus-end

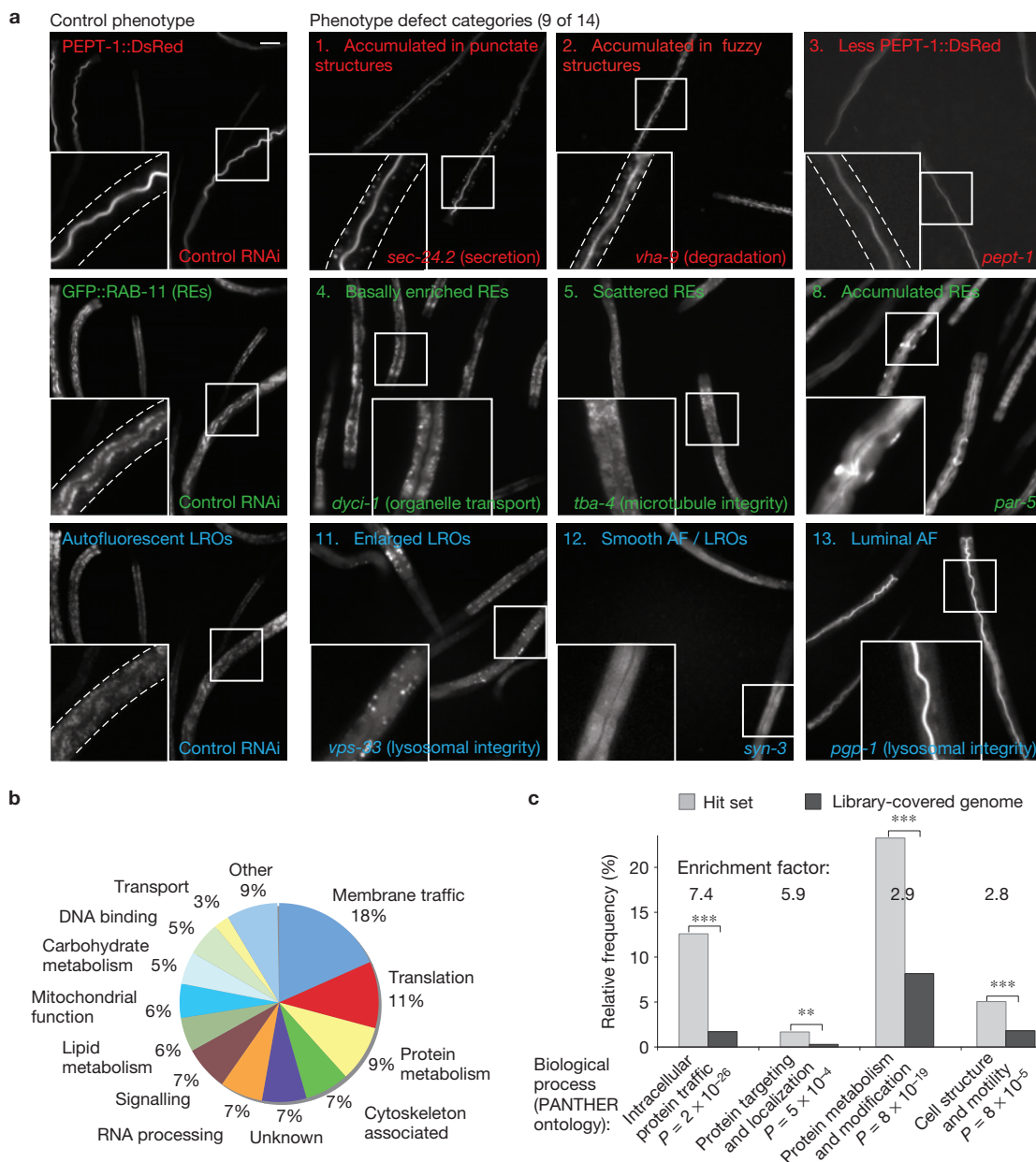


Figure 2 Phenotypic profiling and biological functions of identified genes. **(a)** Representative epifluorescence microscopy images from the primary screen showing the control phenotypes (control RNAi, left-hand column) and nine of the 14 phenotypic defect categories with specific changes in marker distribution, intensity or organelle morphology. Scale bar, 50 μm , and 20 μm for the enlarged view. Perturbations of specific biological functions in membrane trafficking are coupled to specific phenotypic defect categories, as indicated by the gene name and the respective biological function in parentheses. RE, recycling endosome.

microtubule transport and apical enrichment of RAB-11-REs, (2) steady state positioning of endosomes and (3) apical membrane transport.

par-1 and *par-5* RNAi misplace RAB-11-REs

In unpolarized cells, depletion of PAR-6 or the Rho GTPase CDC-42 specifically affects the positioning of RAB-11 and RME-1-positive recycling endosomes⁴⁰. Surprisingly, in *C. elegans* enterocytes, RNAi of *par-3* or *par-6* scattered all types of endosome tested (recycling

(b) Distribution of functional classes in the complete hit set (356 hits). **(c)** Relative frequencies of biological process terms in the complete hit set and the library-covered genome based on the PANTHER Classification System. The x axis shows biological process terms that are over 2.5-fold enriched. The enrichment factor is the ratio of relative frequencies of a term in the hit set over the library-covered genome. 'Intracellular protein traffic' is the most enriched or overrepresented biological process term. Significance levels, ** $P < 0.01$, *** $P < 0.001$; cumulative P -values, hypergeometric distribution.

endosomes, late endosomes, early endosomes; Fig. 3e, group 5). In addition, the GFP-fluorescence intensities of organelle markers were reduced, whereas the apical localization of PEPT-1::DsRed remained unaffected (Fig. 3e). These results suggest that PAR-3 and PAR-6 are of general importance for endosome positioning, possibly through cytoskeletal roles⁹.

Apart from the 'reference gene' SEC-15, group 6 comprised only three candidates causing different Rab11-RE-specific positioning phenotypes, with only weak or no effect on late endosomes, early

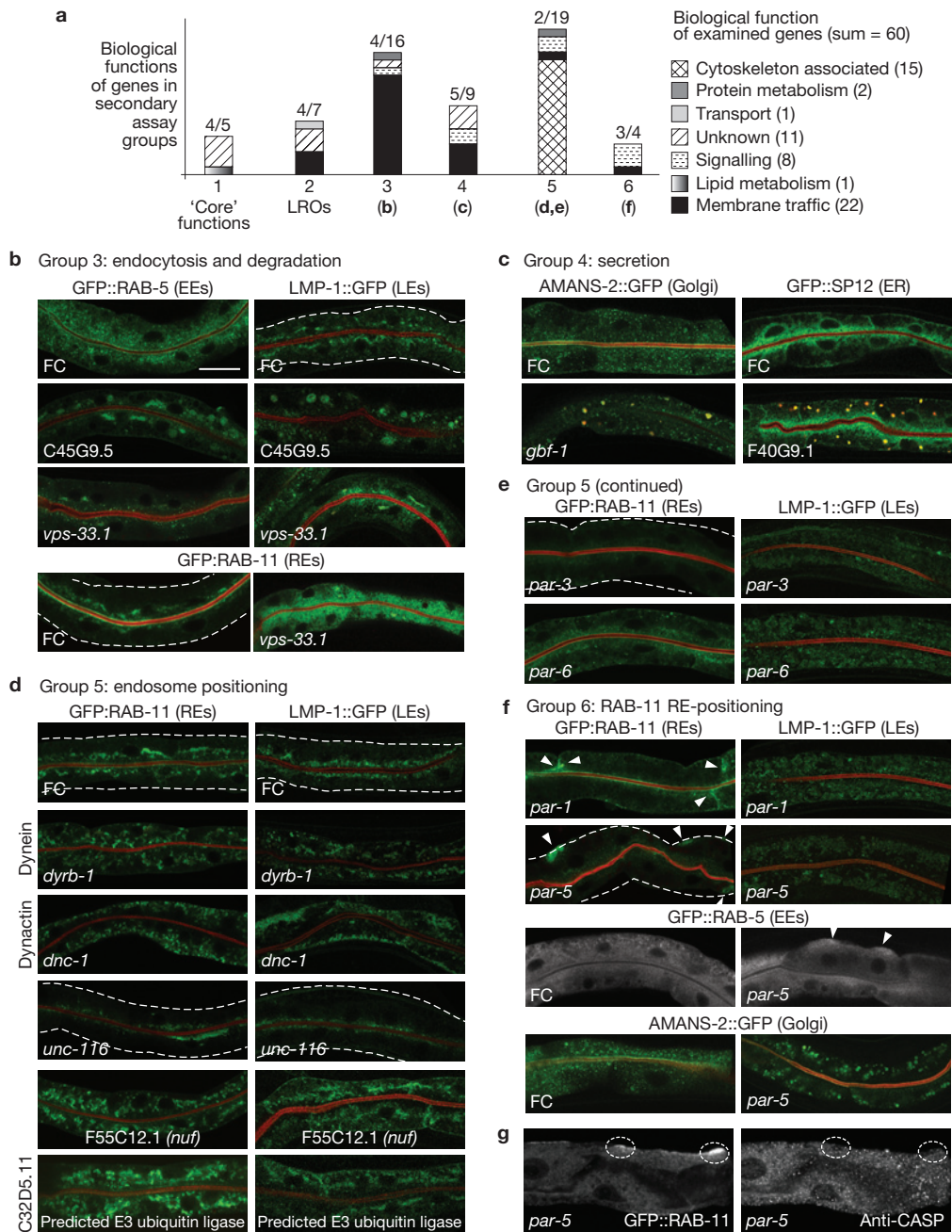


Figure 3 Comparative secondary assays reveal functional roles for candidate genes. **(a)** Compositions of the six functional secondary assay groups. Above each bar, the fraction of genes that was previously not linked to the assigned function is indicated. In total, we proposed functional roles for 22 of the 60 examined genes (for details see Supplementary Table S3). **(b–f)** Confocal microscopy images of RNAi phenotypes representative for four secondary assay groups showing intestinal regions of live secondary assay worms expressing PEPT-1::DsRed (red) and an organelle-specific GFP-marker (green) as indicated above the images. **(b)** RNAi of group 3 genes perturbs endocytosis and early degradation, causing PEPT-1::DsRed accumulations predominantly in early endosomes (EEs) and late endosomes (LEs). *vps-33.1* RNAi also affects recycling endosome morphology and positioning. FC, feeding control. **(c)** RNAi of group 4 genes perturbs secretion and causes PEPT-1::DsRed to accumulate in round, filled structures positive for Golgi and endoplasmic reticulum (ER) markers. **(d)** RNAi of group 5 genes affects different organelles to a similar extent. On perturbation of minus-end-directed microtubule transport, recycling and late endosomes (and early endosomes, not shown) scatter (*dyrb-1* RNAi), or enrich basally

(*dnc-1* RNAi). On depletion of the microtubule plus-end-directed motor UNC-116 (kinesin-1), recycling endosomes and late endosomes concentrate apically in a discontinuous fashion. Both depletion of F55C12.1, the orthologue of the RAB-11 effector NUF, and depletion of the as-yet uncharacterized gene C32D5.11, a predicted E3 ubiquitin ligase, cause scattering of both recycling endosomes and late endosomes. **(e)** Depletion of apical PAR proteins PAR-3 or PAR-6 causes diffuse distribution and reduced GFP-fluorescence intensities of both recycling endosome and late endosome markers. **(f)** RNAi of group 6 genes such as *par-1* and *par-5* affects RAB-11-RE positioning differently, more strongly, or both, than other organelles. Furthermore, and similarly to RNAi of *par-3* and *par-6* **(e)** and *par-1* **(f)**, *par-5* RNAi **(f)** results in a diffuse distribution of late endosomes with reduced fluorescence. Early endosomes and Golgi bodies are affected similarly. However, early endosomes were occasionally observed to cluster weakly at the periphery of these cells (arrowheads). **(g)** *par-5* RNAi-treated, dissected, methanol-fixed intestines immunostained for the endogenous Golgi marker CASP show that Golgi bodies do not enrich at sites of GFP::RAB-11-RE clusters. Scale bar, 20 μ m.

endosomes, or Golgi bodies (Supplementary Table S3, group 6, and Fig. 3f). These were the as-yet uncharacterized WD40 repeat protein H24G06.1 and, unexpectedly, non-apical PAR proteins PAR-1 and PAR-5. Depletion of PAR-1 (ref. 41) resulted in enrichment of RAB-11-REs along cell–cell contact sites (Fig. 3f). Other organelles such as late endosomes were more scattered, and GFP-fluorescence intensities were reduced as for *par-3* and *par-6* RNAi. In the PAR family, PAR-5 (ref. 42) (the orthologue of mammalian 14-3-3 ζ) is functionally its most complex and poorest-understood member. 14-3-3 proteins are dimeric adapters of up to 200 interaction partners, thereby regulating diverse biological functions simultaneously^{43–45}. Depletion of PAR-5 (ref. 42) induced prominent, peripheral clusters of GFP::RAB-11-REs at the basolateral domain of enterocytes (Fig. 3f). In contrast, organelle markers for late endosomes, early endosomes and Golgi bodies (Fig. 3f,g) became diffuse on *par-5* RNAi, with similarly reduced fluorescence intensities as on RNAi of the other *par* genes. Weaker clusters of early endosomes were occasionally observed at the cell periphery (Fig. 3f). Among the tested *par* genes, RNAi of *par-5* caused the strongest effects on intestinal morphology, with more irregularly shaped endotubes and enterocytes (Fig. 3f).

Overall, our results reveal that single depletion of PAR-5 and PAR-1, but not of apical PAR proteins, predominantly affects positioning of RAB-11-REs in enterocytes.

***par-5* RNAi causes recycling endosome clustering around ectopic F-actin**

PAR-5 served as an interesting proof-of-principle candidate for coordinating the interplay between epithelial membrane trafficking, cytoskeleton and cell polarity. Its fly and mammalian orthologue is critical for the localization of PAR3 (ref. 46) and PAR1 (refs 47,48). However, other roles in epithelial polarity remain to be determined. We thus validated and analysed the *par-5* RNAi phenotype in more detail. First, we confirmed the efficient depletion of PAR-5 by RNAi by western blot analysis (Supplementary Fig. S8a). Second, we excluded the possibility that the basal RAB-11-RE clustering was due to RNAi of both *C. elegans* 14-3-3 isoforms, *par-5* (*ftt-1*) and *ftt-2*, which share 80% messenger RNA sequence identity. For this, we used an *ftt-2* deletion strain⁴⁹ (Supplementary Fig. S4a,b) as no viable, temperature sensitive *par-5* strain existed⁴². Third, in non-transgenic worms, recycling endosomes labelled by endogenous RAB-11 also clustered peripherally on *par-5* RNAi (Supplementary Fig. S4m), ruling out a possible epiphenomenon of GFP::RAB-11 expression.

We next asked whether peripherally clustered RAB-11-REs are functionally perturbed, possibly causing accumulation of apical membrane proteins. We examined the localization of PEPT-1::DsRed and the ATP-binding cassette transporter PGP-1::GFP (ref. 50) relative to endogenously labelled RAB-11-REs in control, *arp-1* and *par-5* RNAi (Supplementary Fig. S5). In contrast to RNAi of *arp-1* (dynactin component, positive control), PAR-5 depletion did not cause a significant increase in apical membrane proteins within peripheral recycling endosomes. Notably, we did not observe mis-sorting of PEPT-1::DsRed or PGP-1::GFP to the basolateral membrane on *arp-1* or *par-5* RNAi. These data suggest that alterations in the intracellular positioning of RAB-11-REs do not necessarily perturb cargo trafficking through this compartment.

As 14-3-3 ζ regulates several actin polymerization and depolymerization components^{51–53}, we considered the possibility that the basal clustering of RAB-11-REs results from alterations of the actin cytoskeleton. First, we confirmed that PAR-5 or FTT-1, but not FTT-2, was required for proper microfilament organization (Supplementary Fig. S4c,d). Second, we observed ectopic F-actin patches of varying spread and density at the basolateral cortex, rarely in the central cytoplasm, but not alongside the apical domain (Supplementary Fig. S4i,j,p,q). Virtually all (99%) RAB-11-RE clusters ($n = 145$, in 24 intestines) were located at, or around, ectopic F-actin patches. Unexpectedly, basal GFP::RME-1-labelled recycling endosomes (ref. 24) did not cluster at ectopic F-actin sites but vanished (Supplementary Fig. S4k,l). This interesting observation will require further investigations on the role of PAR-5 for basal recycling endosomes. Third, staining for endogenous markers enabled us to confirm that *par-5* RNAi-induced ectopic F-actin patches were predominantly enriched for clustered RAB-11-REs (88%) and only moderately for RAB-5-labelled early endosomes (26%; Supplementary Fig. S4m–o). Only peripheral RAB-11-REs induced by *par-5* RNAi, not by *arp-1* RNAi, clustered around prominent patches of ectopic F-actin (Fig. 4a–d). This indicated that peripherally clustered recycling endosomes are *per se* insufficient to cause ectopic F-actin accumulation, and that the ectopic F-actin may precede the clustering of RAB-11-REs. This possibility is consistent with the finding that a small but significant fraction of ectopic F-actin patches (12%) was devoid of co-clustered RAB-11-REs. Next, we analysed the effects of PAR-5 depletion on apicobasal F-actin organization and F-actin levels. Two line-based intensity quantification approaches (illustrated in Fig. 4e) revealed a ~ 3.7 -fold increase in mean fluorescence intensity at ectopic basal F-actin sites (Fig. 4f,g), and a moderate but significant reduction (1.2 fold) in mean peak intensities of apical F-actin ($P = 3 \times 10^{-6}$, Wilcoxon rank sum test) in *par-5* RNAi when compared with control. This was coupled to more irregularly shaped endotubes (compare Fig. 4a,b), suggesting that PAR-5 depletion also altered apical F-actin organization. Although the integral F-actin intensities of these line-based measures were slightly increased in *par-5* RNAi enterocytes (1.2-fold) ($P = 0.013$, Wilcoxon rank sum test), area-based intensity measurements revealed that the total F-actin levels were not significantly changed (control, 31 intestines; *par-5* RNAi, 45 intestines; $P = 0.92$, Wilcoxon rank sum test). When compared with PAR-5 depletion, depletion of the actin depolymerizing factor (ADF)/cofilin orthologue UNC-60 (ref. 54), a key F-actin regulator and target of 14-3-3 ζ (ref. 51), caused RAB-11-RE clustering preferentially at apical ectopic microfilaments (Supplementary Fig. S4r,s). Altogether, the effects of PAR-5 depletion together with the ADF/cofilin RNAi phenotype underscore the importance of proper apicobasal F-actin organization for RAB-11-RE positioning.

RAB-11-RE clusters coincide with ectopic apical components

We next inspected whether other apical domain components were enriched at the ‘ectopic sites’ with clustered GFP::RAB-11-REs and peripheral F-actin. The F-actin membrane linker ERM-1 (refs 25,27), the signalling adaptor and barbed-end capping protein EPS-8 (ref. 55), the intermediate filament protein IFB-2 (ref. 56) and the apical junction protein AJM-1 (ref. 57) all accumulated at the cortical sites where GFP::RAB-11-REs clustered (Fig. 5). γ -tubulin also enriched

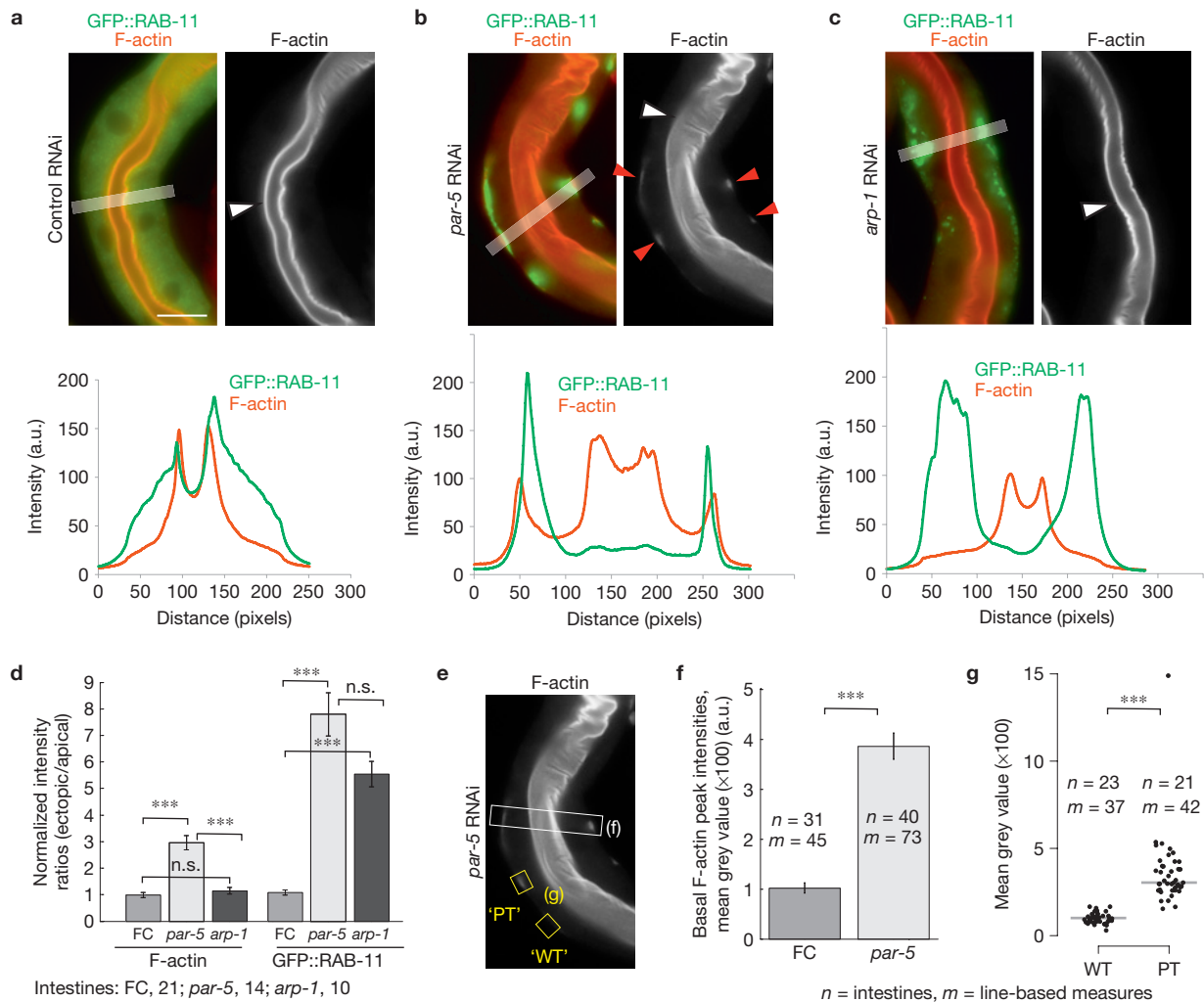


Figure 4 PAR-5 depletion causes RAB-11-REs to cluster around ectopic F-actin at the basolateral cortex. (a–c) GFP::RAB-11-expressing and rhodamine phalloidin-stained intestines treated with control, *par-5* and *arp-1* RNAi, as well as intensity diagrams corresponding to the indicated lines. To improve the visualization of ectopic F-actin, the brightness and contrast of each grey image was increased. Scale bar, 20 μm . (a) In control RNAi, rhodamine phalloidin-labelled F-actin is strongly concentrated at the apical domain (white arrowhead) and not visible at the basal domain or cell periphery. (b) On PAR-5 depletion, GFP::RAB-11-labelled recycling endosomes cluster peripherally around patches of ectopic F-actin (red arrowheads) at the basolateral cortex. The endotube labelled by apical F-actin (white arrowhead) can become more dilated and irregularly shaped on *par-5* RNAi. (c) In *arp-1* RNAi intestines, peripheral GFP::RAB-11-labelled recycling endosomes do not coincide with ectopic F-actin patches. (d) Comparison of mean peak intensity ratios of ectopic:apical F-actin (left) and ectopic (or basal):apical

GFP::RAB-11 (right) for line-based intensity measures collected from control, *par-5* and *arp-1* RNAi-treated intestines. When compared with control and *arp-1* RNAi, the ectopic:apical F-actin intensity ratio in *par-5* RNAi is increased threefold. The ectopic:apical GFP::RAB-11 intensity ratios in *par-5* and *arp-1* RNAi are similarly increased. FC, feeding control. (e) Illustration of two methods of line-based intensity measurement of rhodamine phalloidin-stained F-actin. (f) Lines perpendicular across control RNAi and phenotypic *par-5* RNAi intestines reveal a 3.8-fold increase in basal F-actin mean peak intensities. (g) Lines along selected regions at the basal cell periphery of *par-5* RNAi-treated intestines reveal a 3.6-fold increase in mean basal F-actin intensities at sites with ectopic F-actin patches ('PT') when compared with those without ('WT'). Individual measurements m are plotted as black dots; the grey line indicates the median. Significance level, *** $P < 0.001$; Wilcoxon rank sum test. Error bars in d and f, s.e.m., derived using the m values. The number of intestines n in d, f and g derives from up to three experiments.

moderately at these sites (Fig. 5g–i), possibly accounting for the microtubule arrays occasionally observed around recycling endosome clusters (Supplementary Fig. S6g,n). In *C. elegans* one-cell embryos, proper cortical localization of anterior PAR proteins and regulation of the actomyosin meshwork are functionally interdependent^{9,58}. Are apical PAR proteins also enriched at the ectopic sites on PAR-5 depletion? In control adult intestines, apical PAR proteins concentrated at the apical domain (PKC-3 or aPKC) and along AJM-1-labelled apical junctions (PAR-6, PAR-3), but not at the

basolateral cortex (Supplementary Fig. S7b,h,n). Visualization of endogenous PAR-3 by immunofluorescence proved, however, difficult, presumably owing to its low expression levels in adult intestines¹¹. In contrast, over 83% of *par-5* RNAi-treated intestines exhibited ectopically enriched PKC-3, PAR-6 and PAR-3 at the basolateral cortex adjacent to peripherally clustered GFP::RAB-11-REs and ectopic AJM-1 (Supplementary Fig. S7e,k,q,t). These results show that PAR-5 is critical to maintain apicobasal asymmetry of apical domain components.

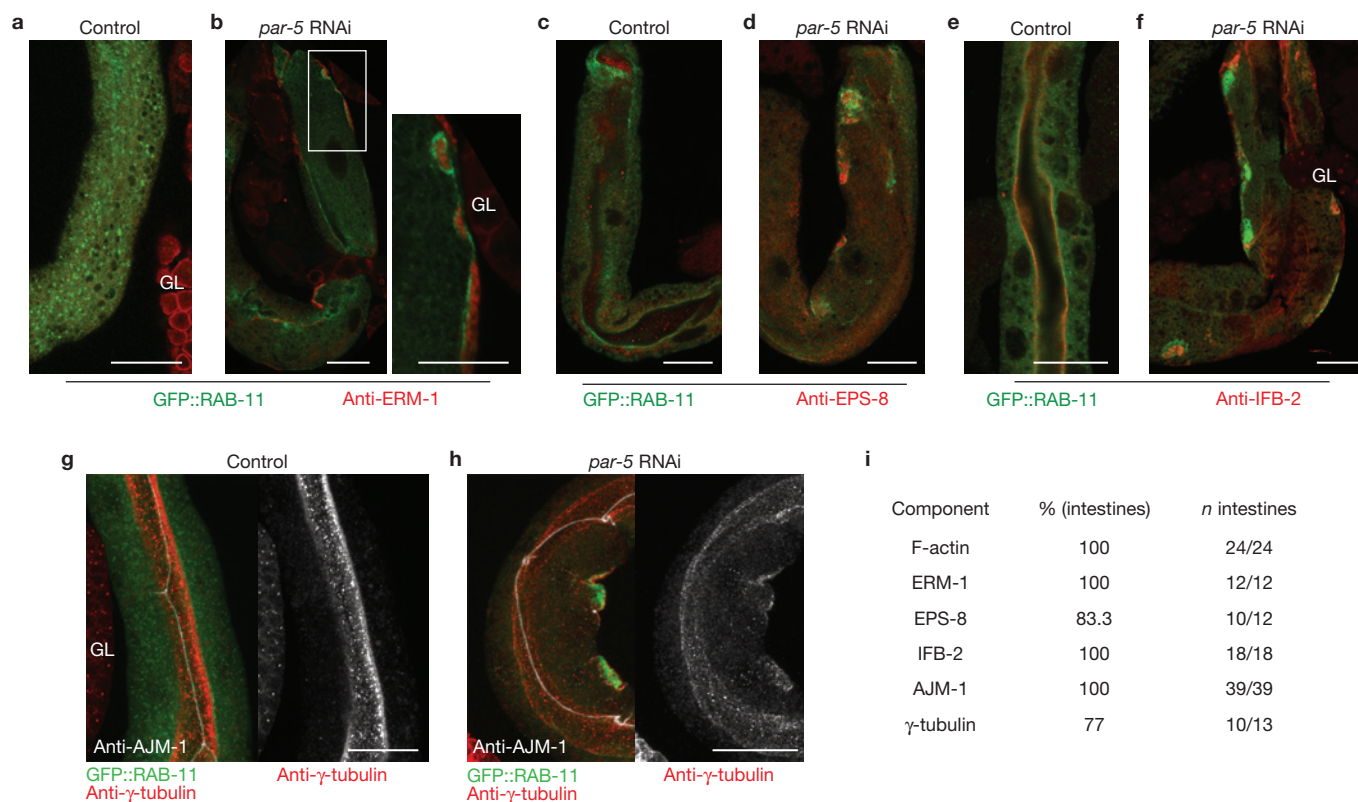


Figure 5 RAB-11-REs cluster at ectopic sites at the basolateral cortex that are enriched for various apical domain components. (a–h) GFP::RAB-11-expressing, control and *par-5* RNAi-treated intestines immunostained for various apical cytoskeleton components, such as the F-actin binding proteins ERM-1 (a–b) and EPS-8 (c,d) as well as intermediate filament protein IFB-2 (e,f). Images show single confocal microscopy sections with more peripheral (a) or medial (e) views of the intestines. GL, germline. Note that, in *PAR-5*-depleted intestines only, these apical cytoskeleton components co-accumulate ectopically at the basolateral cortex at sites where GFP::RAB-11-labelled recycling endosomes cluster. (g,h) Intestines immunostained for AJM-1 and

γ-tubulin on control and *par-5* RNAi (maximum intensity projections, seven consecutive confocal sections). (g) AJM-1 demarcates apical junctions, and γ-tubulin-containing complexes are part of the apical cytoskeleton, concentrating around the endotube. (h) In *par-5* RNAi intestines, AJM-1 and γ-tubulin-containing complexes localize ectopically to cortical sites with peripherally clustered GFP::RAB-11-labelled recycling endosomes. (i) Mean percentage of *par-5* RNAi-treated intestines with peripherally clustered GFP::RAB-11-REs at which the indicated apical domain components co-accumulated ectopically. *n* derives from up to four independent experiments. Scale bar in enlarged box of b, 10 μm; all others, 20 μm.

par-5 phenotype requires apical PARs and Rho GTPases

To identify key factors required for ectopic site formation, we tested whether ectopic F-actin and recycling endosome clusters are prevented on double depletion of *PAR-5* with regulators of F-actin dynamics and cell polarity, such as Rho GTPases and apical PAR proteins^{2,10}. To this end, we carried out double-feeding experiments, with *par-5* plus scrambled double-stranded RNA (dsRNA) (*par-5* + feeding control) as reference. Notably, all double depletions (*par-5* + second gene) significantly reduced the *par-5* RNAi phenotype frequency, that is the mean percentage of intestines with one or more peripheral GFP::RAB-11-RE clusters (Fig. 6b). Among the tested Rho GTPases, double depletion of *PAR-5* with *RHO-1* or *CED-10* (*Rac1* orthologue) efficiently suppressed recycling endosome clustering (up to 49-fold), whereas double depletion of *PAR-5* with *CDC-42* was less effective (2.7-fold suppression). Furthermore, intestines in the reference sample exhibited more and larger ectopic F-actin patches than those in the test samples (Fig. 6c–e). The modest clustering-suppression by *CDC-42* co-depletion could be due to additive phenotypic effects, as single depletion of *CDC-42* also caused small ectopic F-actin patches co-clustered with GFP::RAB-11-REs (not shown). In contrast to *cdc-42* RNAi, we did not observe ectopic

F-actin structures or recycling endosome clusters on RNAi of *ced-10*, *rho-1*, *par-3* or *par-6*. However, depletion of *CED-10* (*Rac1*) reduced the fluorescence intensity of GFP::RAB-11 (not shown). Overall, these data demonstrate that Rho GTPases, specifically *RHO-1* and *CED-10* (*Rac1*), as well as apical PAR proteins, (1) are required for the formation of both ectopic F-actin and RAB-11-RE clusters on *PAR-5* depletion and (2) need *PAR-5* to properly maintain apicobasal asymmetry.

DISCUSSION

Here, we carried out an *in vivo* RNAi screen in *C. elegans* intestine for genes maintaining apical enrichment of RAB-11-REs and apical membrane transport. In contrast to previous *C. elegans* RNAi screens for membrane-transport regulators^{26,40}, three subcellular readouts were simultaneously monitored, that is PEPT-1::DsRed, GFP::RAB-11 and LROs. Using a semi-automated workflow with epifluorescence microscopy and custom-made image analysis, we employed advanced HCS technologies mainly used in cell-based assays on live animals⁵⁹. The primary screen with 356 hits is a rich information resource, comprising phenotype profiles, biological functions, protein domain and orthologue annotations

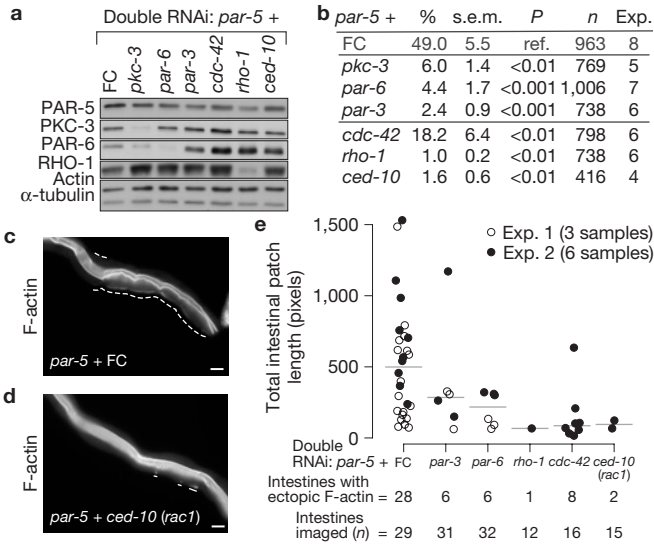


Figure 6 Formation of peripheral GFP::RAB-11-RE clusters and ectopic F-actin patches on depletion of PAR-5 depends on both Rho GTPases and apical PAR proteins. **(a)** In each experiment, we confirmed that all double RNAi samples—that is, reference (*par-5* + feeding control bacteria (FC)) and test (*par-5* + apical *par* gene or *rho* GTPase gene) samples—have similar levels of PAR-5 depletion as indicated by similar PAR-5 to α -tubulin ratios in total worm protein extracts. One representative western blot is shown. Concomitantly, we confirmed the efficient depletion of PKC-3, PAR-6 and RHO-1, as well as CDC-42 (GFP::CDC-42), in the respective test samples. Bands were cropped from three blots: α -tubulin, actin and RHO-1 from one; PAR-5 from a second; and PKC-3 and PAR-6 from a third (see Supplementary Fig. S8 for uncropped western blots and probing for GFP::CDC-42). **(b)** Epifluorescence-microscopy-based quantification of the mean percentage of phenotypic worms with one or more peripheral GFP::RAB-11-RE clusters after double RNAi with *par-5*. *P*-values relative to reference (ref.), Wilcoxon rank sum test. *n*, number of analysed worms. In all test samples, recycling endosome clustering was suppressed. **(c–e)** Comparison of the phenotype strength in affected intestines of reference and test samples. Epifluorescence images of rhodamine phalloidin-stained, double-RNAi-treated intestines with ectopic F-actin patches. The dashed lines illustrate the different total ectopic F-actin patch lengths per imaged intestine that result from the total number and length of patches. Scale bars, 20 μ m. **(e)** Box plots with overlaid individual data points of two independent experiments (filled and open circles) of the total measured length of ectopic F-actin patches per phenotypic intestine. All test samples exhibit considerably reduced medians (indicated by grey lines) of total ectopic patch length values. For this analysis, we selected from each double-RNAi sample phenotypic worms with clustered recycling endosomes—if these were present—or else we selected worms with defective germlines indicative of *par-5* RNAi. Underneath the *x* axis, the numbers of intestines with ectopic F-actin patches and the total number of analysed worms (*n*) are shown, with *n* deriving from one or two experiments.

(Supplementary Table S1). Functional predictions inferred from hierarchical clustering for 22 genes were validated in secondary assays (Supplementary Table S3). Overall, both primary and secondary assay data sets revealed numerous candidate genes with a potential role in epithelial cell polarity.

We further garnered mechanistic insights into the regulation of RAB-11-RE positioning and epithelial cell polarity. First, RAB-11-RE positioning requires the dynein–dynactin complexes, regulatory components and kinesin-1. Therefore, our findings in *C. elegans* enterocytes suggest that their orthologues in higher-metazoan epithelia also mediate transport and apical enrichment of Rab11-REs. Unexpectedly, deletion of the myosin Vb (ref. 60) orthologue HUM-2

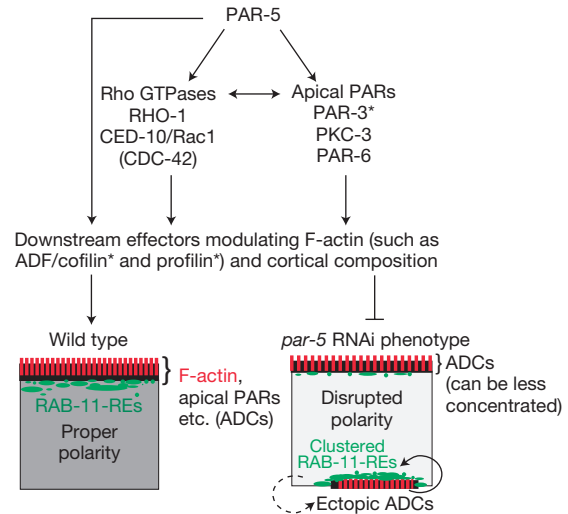


Figure 7 Functional PAR-5 model. PAR-5 maintains apicobasal polarity by functioning as a regulatory hub for the coordinated interplay of Rho GTPases, apical PAR proteins and downstream effectors. Network components that could require direct regulatory interaction with PAR-5, such as PAR-3 (ref. 46) and numerous F-actin-modulating downstream effectors (ADF/cofilin^{51,52}, profilin⁶² and possibly orthologues of cofilin kinase⁵² and phosphatase⁵³), are labelled by asterisks. Arrows indicate regulatory effects that can be mutual (double arrows). Other roles or effects, as well as crosstalk of network components, are not indicated. PAR-5 sustains proper F-actin dynamics and asymmetry of F-actin and other apical domain components (labelled as ADCs), and allows for microtubule-dependent enrichment of RAB-11-REs (wild type, left-hand cell, PAR-5 in grey). Single depletion of PAR-5, and thus deregulation of this polarity-maintaining network, causes ectopic sites at the basolateral cortex, comprising F-actin and other apical domain components, as well as strongly clustered RAB-11-REs (*par-5* RNAi phenotype, right-hand cell, light grey for depleted PAR-5). Double depletion of PAR-5 with one of the Rho GTPases or apical PAR proteins suppressed both ectopic F-actin and recycling endosome clustering efficiently (or moderately in the case of CDC-42), indicating that ectopic F-actin and apical domain components induce the local clustering of RAB-11-REs (circular arrow). RAB-11-REs could also feed back on ectopic F-actin formation (dashed circular arrow), thereby enhancing the peripheral clustering. See Discussion for further details.

did not significantly alter RAB-11-RE distribution (data not shown), which may be due to functional redundancy.

Second, we revealed a previously unknown role of PAR-5 in apicobasal polarity and RAB-11-RE positioning. Depletion of PAR-5 induced the formation of ectopic sites at the basolateral cortex including F-actin and other structural and regulatory apical domain components (ERM-1, EPS-8, IFB-2, γ -tubulin, AJM-1 and the apical PAR proteins PKC-3, PAR-6 and PAR-3), as well as clustered RAB-11-REs. In contrast, depletion of apical PAR proteins or Rho GTPases did not cause prominent polarity- or organelle-specific positioning phenotypes. Thus, although seemingly robust, epithelial polarity relies on regulatory hub proteins, such as PAR-5, that coordinate numerous components and functions simultaneously. For example, the mammalian PAR-5 orthologue 14-3-3 ζ regulates several key proteins for cytoskeletal organization and polarity, such as Rho guanine nucleotide exchange factors (GEFs) and GTPase-activator proteins (refs 61,62), PAR3 (ref. 46) and components of the core machinery for F-actin dynamics that are downstream effectors predominantly of RhoA (RHO-1) and Rac1, but also Cdc42 (refs 45,62). These include ADF/cofilin⁵¹, profilin⁶², the ADF/cofilin regulatory kinase LIMK (ref. 52), which

is inhibited by PAR3 (ref. 63), and the ADF/cofilin phosphatase SSH (ref. 64). Importantly, double depletion of PAR-5 with each apical PAR protein, RHO-1 or CED-10 (Rac1) strongly suppressed both ectopic F-actin patches and RAB-11-RE clusters, suggesting that all these factors contribute interdependently to the formation of ectopic sites. By integrating published findings with our results, we propose the following model for the role of PAR-5 in epithelial polarity maintenance (Fig. 7). Under physiological conditions, PAR-5 constitutes a regulatory hub (or nodal point) for a cell polarity-protein network including Rho GTPases (RHO-1, CED-10 (Rac1) and CDC-42), apical PAR proteins (PKC-3, PAR-6 and PAR-3) and F-actin modulating downstream effectors. Such interactions are critical to maintain the low net levels of F-actin and other apical domain components at the basolateral cortex. In the presence of PAR-5, transport and apical enrichment of RAB-11-REs depends primarily on the microtubule-based machinery. *par-5* depletion perturbs the cell polarity regulatory network: altered F-actin dynamics and de-regulated activities of Rho GTPases, as well as ectopically localized apical PAR proteins, then cause the formation of the ectopic sites at the basolateral cortex that is susceptible to capturing or forming ectopic microfilaments^{65–67}.

The prominent, peripheral clustering of RAB-11-REs around ectopic F-actin patches could be accounted for by a number of non-exclusive mechanisms. First, altered F-actin dynamics and ectopic microfilaments could functionally interfere with proteins that mediate positioning of RAB-11-REs, such as specific motor proteins or cytoskeletal adaptors. This interpretation is further supported by RNAi of *unc-60* (ref. 54; ADF/cofilin, Supplementary Fig. S4r,s), which also caused ectopic microfilaments and co-clustered RAB-11-REs. Second, recycling-endosome-specific positioning factors could functionally depend on regulatory interactions with PAR-5 and, on its depletion, cause recycling endosome clustering or fail to enrich recycling endosomes apically (such as potentially dynein heavy chain and NUDEL (ref. 62; NUD-2)). Third, in the condition of altered F-actin dynamics, clustering RAB-11-REs and ectopic microfilament formation may positively influence each other, thus exacerbating the phenotype. Several previously identified factors localized to Rab11-REs could facilitate this, such as the Rab11 effector NUF (ref. 68), actin nucleation factors⁶⁹, Cdc42 (ref. 70), PAR-6 (ref. 40) and microfilament tethering motors such as myosin Vb (ref. 60; HUM-2).

It will be important for future research to further elucidate how the polarity-maintaining protein network of which PAR-5 is a central element functions in coordinating apicobasal polarity and the functional properties of membrane organelles such as RAB-11-REs. Our proof-of-principle analysis of PAR-5 demonstrates that the genes identified in our screen can provide important molecular insights into the mechanisms underlying organelle positioning and apical membrane transport, as well as polarity maintenance. □

METHODS

Methods and any associated references are available in the online version of the paper at www.nature.com/naturecellbiology

Note: Supplementary Information is available on the Nature Cell Biology website

ACKNOWLEDGEMENTS

We thank various members of the HT-TDS including J. Wagner, M. Gieth and H. Grabner for assistance in development and robotic programming of automation steps of the screening workflow. We are very grateful to M. Storch, U. Frömmel,

T. Döbel, L. Socher, S. Quaiser, S. Scheibe, F. Zakrezweski and D. Haase for their assistance throughout the primary HCS. We thank R. Schäfer for technical assistance. We are grateful to S. Eaton, K. Simons, E. Knust, E. Paluch, G. A. O'Sullivan, N. Goehring and B. Habermann for discussions and critical reading of the manuscript draft and to C. Eckmann for protocols and practical advice.

This study was supported by the German Federal Ministry of Education and Research (InnoRegio Initiative, grant number 0314035A; the Systems Biology Network HepatoSys, grant number 0313082H, and the Virtual Liver initiative, www.virtual-liver.de), the EU sixth framework project 'EndoTrack' (FP6 Grant LSHG-CT-2006-019050) and the Max Planck Society's inter-institutional initiative 'RNA interference'. J.F.W. was supported by a PhD fellowship of the Boehringer Ingelheim Fonds.

AUTHOR CONTRIBUTIONS

S.H. and M.Z. conceived the initial concept for the screen. S.H. established the screening platform with support from J.F.W. S.H. and J.F.W. conducted the genome-wide screen with the support of K.K., students from the Technical University Dresden and staff members from the High-Throughput Technology Development Studio (HT-TDS; see Acknowledgements). S.H. developed the image analysis software. J.F.W. conceived the embryonic lethal screen and conducted it with support from S.H. and students. S.H., J.F.W. and M.Z. analysed the data with the help of B.H., C.R.B. (general bioinformatics) and M.V. (hierarchical clustering). J.F.W. carried out secondary assays with the support of B.O.F. J.F.W. conceived, carried out and analysed the experiments on PAR-5. G.M. contributed to quantifications and statistical analysis on PAR-5. J.F.W. and M.Z. wrote the manuscript with the contribution of S.H., G.M., C.R.B. and M.V.

COMPETING FINANCIAL INTERESTS

The authors declare no competing financial interests.

Published online at www.nature.com/naturecellbiology

Reprints and permissions information is available online at www.nature.com/reprints

1. Apodaca, G. Endocytic traffic in polarized epithelial cells: role of the actin and microtubule cytoskeleton. *Traffic* **2**, 149–159 (2001).
2. Iden, S. & Collard, J. G. Crosstalk between small GTPases and polarity proteins in cell polarization. *Nat. Rev. Mol. Cell Biol.* **9**, 846–859 (2008).
3. Knust, E. & Bossinger, O. Composition and formation of intercellular junctions in epithelial cells. *Science* **298**, 1955–1959 (2002).
4. Goldenring, J. R. *et al.* Rab11 is an apically located small GTP-binding protein in epithelial tissues. *Am. J. Physiol.* **270**, G515–G525 (1996).
5. Rodriguez-Boulant, E., Kreitzer, G. & Musch, A. Organization of vesicular trafficking in epithelia. *Nat. Rev. Mol. Cell Biol.* **6**, 233–247 (2005).
6. Mellman, I. & Nelson, W. J. Coordinated protein sorting, targeting and distribution in polarized cells. *Nat. Rev. Mol. Cell Biol.* **9**, 833–845 (2008).
7. Bryant, D. M. & Mostov, K. E. From cells to organs: building polarized tissue. *Nat. Rev. Mol. Cell Biol.* **9**, 887–901 (2008).
8. Suzuki, A. & Ohno, S. The PAR–aPKC system: lessons in polarity. *J. Cell Sci.* **119**, 979–987 (2006).
9. Munro, E. PAR proteins and the cytoskeleton: a marriage of equals. *Curr. Opin. Cell Biol.* **18**, 86–94 (2006).
10. Nance, J. & Zallen, J. A. Elaborating polarity: PAR proteins and the cytoskeleton. *Development* **138**, 799–809 (2011).
11. Achilleos, A., Wehman, A. M. & Nance, J. PAR-3 mediates the initial clustering and apical localization of junction and polarity proteins during *C. elegans* intestinal epithelial cell polarization. *Development* **137**, 1833–1842 (2010).
12. Totong, R., Achilleos, A. & Nance, J. PAR-6 is required for junction formation but not apicobasal polarization in *C. elegans* embryonic epithelial cells. *Development* **134**, 1259–1268 (2007).
13. Daley, W. P. *et al.* ROCK1-directed basement membrane positioning coordinates epithelial tissue polarity. *Development* **139**, 411–422 (2012).
14. Etienne-Manneville, S. & Hall, A. Rho GTPases in cell biology. *Nature* **420**, 629–635 (2002).
15. Zerial, M. & McBride, H. Rab proteins as membrane organizers. *Nat. Rev. Mol. Cell Biol.* **2**, 107–117 (2001).
16. Lundquist, E. A. Small GTPases (January 17, 2006), *WormBook*, ed. The *C. elegans* Research Community, WormBook, <http://dx.doi.org/10.1895/wormbook.1.67.1>, <http://www.wormbook.org>.
17. Golachowska, M. R., Hoekstra, D. & van, I. S. C. Recycling endosomes in apical plasma membrane domain formation and epithelial cell polarity. *Trends Cell Biol.* **20**, 618–626 (2010).
18. Shivas, J. M., Morrison, H. A., Bilder, D. & Skop, A. R. Polarity and endocytosis: reciprocal regulation. *Trends Cell Biol.* **20**, 445–452 (2010).
19. Prekeris, R., Klumperman, J. & Scheller, R. H. A Rab11/Rip11 protein complex regulates apical membrane trafficking via recycling endosomes. *Mol. Cell* **6**, 1437–1448 (2000).

20. Swiatecka-Urban, A. *et al.* Myosin Vb is required for trafficking of the cystic fibrosis transmembrane conductance regulator in Rab11a-specific apical recycling endosomes in polarized human airway epithelial cells. *J. Biol. Chem.* **282**, 23725–23736 (2007).
21. Langevin, J. *et al.* Drosophila exocyst components Sec5, Sec6, and Sec15 regulate DE-Cadherin trafficking from recycling endosomes to the plasma membrane. *Dev. Cell* **9**, 355–376 (2005).
22. Ang, A. L. *et al.* Recycling endosomes can serve as intermediates during transport from the Golgi to the plasma membrane of MDCK cells. *J. Cell Biol.* **167**, 531–543 (2004).
23. Wu, S., Mehta, S., Pichaud, F., Bellen, H. & Quiocho, F. Sec15 interacts with Rab11 via a novel domain and affects Rab11 localization *in vivo*. *Nat. Struct. Mol. Biol.* **12**, 879–885 (2005).
24. Chen, C. C. *et al.* RAB-10 is required for endocytic recycling in the *Caenorhabditis elegans* intestine. *Mol. Biol. Cell* **17**, 1286–1297 (2006).
25. Zhang, H. *et al.* Apicobasal domain identities of expanding tubular membranes depend on glycosphingolipid biosynthesis. *Nat. Cell Biol.* **13**, 1189–1201 (2011).
26. Hermann, G. J. *et al.* Genetic analysis of lysosomal trafficking in *Caenorhabditis elegans*. *Mol. Biol. Cell* **16**, 3273–3288 (2005).
27. Van Fürden, D., Johnson, K., Segbert, C. & Bossinger, O. The *C. elegans* ezrin–radixin–moesin protein ERM-1 is necessary for apical junction remodelling and tubulogenesis in the intestine. *Developmental Biol.* **272**, 262–276 (2004).
28. McGhee, J. D. The *C. elegans* intestine (March 27, 2007), *WormBook*, ed. The *C. elegans* Research Community, *WormBook*, <http://dx.doi.org/10.1895/wormbook.1.133.1>, <http://www.wormbook.org>.
29. McGhee, J. D. The *C. elegans* intestine. *WormBook* 1–36 (2007).
30. Nehrke, K. A reduction in intestinal cell pH_i due to loss of the *Caenorhabditis elegans* Na⁺/H⁺ exchanger NHX-2 increases life span. *J. Biol. Chem.* **278**, 44657–44666 (2003).
31. Casanova, J. E. *et al.* Association of Rab25 and Rab11a with the apical recycling system of polarized Madin–Darby canine kidney cells. *Mol. Biol. Cell* **10**, 47–61 (1999).
32. Kamath, R. S. & Ahringer, J. Genome-wide RNAi screening in *Caenorhabditis elegans*. *Methods* **30**, 313–321 (2003).
33. Blum, H. *Models for the Perception of Speech and Visual Forms* 362–380 (MIT Press, 1967).
34. Thomas, P. *et al.* PANTHER: a browsable database of gene products organized by biological function, using curated protein family and subfamily classification. *Nucleic Acids Res.* **31**, 334–341 (2003).
35. Johnson, S. C. Hierarchical clustering schemes. *Psychometrika* **32**, 241–254 (1967).
36. McGary, K. L., Lee, I. & Marcotte, E. M. Broad network-based predictability of *Saccharomyces cerevisiae* gene loss-of-function phenotypes. *Genome Biol.* **8**, R258 (2007).
37. Kardon, J. R. & Vale, R. D. Regulators of the cytoplasmic dynein motor. *Nat. Rev. Mol. Cell Biol.* **10**, 854–865 (2009).
38. Horgan, C. P., Hanscom, S. R., Jolly, R. S., Futter, C. E. & McCaffrey, M. W. Rab11-FIP3 links the Rab11 GTPase and cytoplasmic dynein to mediate transport to the endosomal-recycling compartment. *J. Cell Sci.* **123**, 181–191 (2010).
39. Arimoto, M. *et al.* The *Caenorhabditis elegans* JIP3 protein UNC-16 functions as an adaptor to link kinesin-1 with cytoplasmic dynein. *J. Neurosci.* **31**, 2216–2224 (2011).
40. Balklava, Z., Pant, S., Fares, H. & Grant, B. D. Genome-wide analysis identifies a general requirement for polarity proteins in endocytic traffic. *Nat. Cell Biol.* **9**, 1066–1073 (2007).
41. Guo, S. & Kempfues, K. J. par-1, a gene required for establishing polarity in *C. elegans* embryos, encodes a putative Ser/Thr kinase that is asymmetrically distributed. *Cell* **81**, 611–620 (1995).
42. Morton, D. *et al.* The *Caenorhabditis elegans* par-5 gene encodes a 14-3-3 protein required for cellular asymmetry in the early embryo. *Dev. Biol.* **241**, 47–58 (2002).
43. Jin, J. *et al.* Proteomic, functional, and domain-based analysis of *in vivo* 14-3-3 binding proteins involved in cytoskeletal regulation and cellular organization. *Curr. Biol.* **14**, 1436–1450 (2004).
44. Pozuelo Rubio, M. *et al.* 14-3-3-affinity purification of over 200 human phosphoproteins reveals new links to regulation of cellular metabolism, proliferation and trafficking. *Biochem. J.* **379**, 395–408 (2004).
45. Angrand, P. O. *et al.* Transgenic mouse proteomics identifies new 14-3-3-associated proteins involved in cytoskeletal rearrangements and cell signaling. *Mol. Cell Proteomics* **5**, 2211–2227 (2006).
46. Hurd, T. *et al.* Phosphorylation-dependent binding of 14-3-3 to the polarity protein Par3 regulates cell polarity in mammalian epithelia. *Curr. Biol.* **13**, 2082–2090 (2003).
47. Benton, R. & St Johnston, D. Drosophila PAR-1 and 14-3-3 inhibit Bazooka/PAR-3 to establish complementary cortical domains in polarized cells. *Cell* **115**, 691–704 (2003).
48. Kusakabe, M. & Nishida, E. The polarity-inducing kinase Par-1 controls *Xenopus* gastrulation in cooperation with 14-3-3 and aPKC. *EMBO J.* **23**, 4190–4201 (2004).
49. Berdichevsky, A., Viswanathan, M., Horvitz, H. R. & Guarente, L. *C. elegans* SIR-2.1 interacts with 14-3-3 proteins to activate DAF-16 and extend life span. *Cell* **125**, 1165–1177 (2006).
50. Sato, T. *et al.* The Rab8 GTPase regulates apical protein localization in intestinal cells. *Nature* **448**, 366–369 (2007).
51. Gohla, A. & Bokoch, G. M. 14-3-3 regulates actin dynamics by stabilizing phosphorylated cofilin. *Curr. Biol.* **12**, 1704–1710 (2002).
52. Birkenfeld, J., Betz, H. & Roth, D. Identification of cofilin and LIM-domain-containing protein kinase 1 as novel interaction partners of 14-3-3 ζ . *Biochem. J.* **369**, 45–54 (2003).
53. Nagata-Ohashi, K. *et al.* A pathway of neuregulin-induced activation of cofilin-phosphatase Slingshot and cofilin in lamellipodia. *J. Cell Biol.* **165**, 465–471 (2004).
54. Ono, K., Parast, M., Alberico, C., Benian, G. & Ono, S. Specific requirement for two ADF/cofilin isoforms in distinct actin-dependent processes in *Caenorhabditis elegans*. *J. Cell Sci.* **116**, 2073–2085 (2003).
55. Croce, A. *et al.* A novel actin barbed-end-capping activity in EPS-8 regulates apical morphogenesis in intestinal cells of *Caenorhabditis elegans*. *Nat. Cell Biol.* **6**, 1173–1179 (2004).
56. Hüsken, K. *et al.* Maintenance of the intestinal tube in *Caenorhabditis elegans*: the role of the intermediate filament protein IFC-2. *Differentiation* **76**, 881–896 (2008).
57. Koppen, M. *et al.* Cooperative regulation of AJM-1 controls junctional integrity in *Caenorhabditis elegans* epithelia. *Nat. Cell Biol.* **3**, 983–991 (2001).
58. Cowan, C. R. & Hyman, A. A. Asymmetric cell division in *C. elegans*: cortical polarity and spindle positioning. *Annu. Rev. Cell Dev. Biol.* **20**, 427–453 (2004).
59. Boutros, M. & Ahringer, J. The art and design of genetic screens: RNA interference. *Nat. Rev. Genetics* **9**, 554–566 (2008).
60. Provance, W. *et al.* Myosin-Vb functions as a dynamic tether for peripheral endocytic compartments during transferrin trafficking. *BMC Cell Biol.* **9**, 44 (2008).
61. Zenke, F. T. *et al.* p21-activated kinase 1 phosphorylates and regulates 14-3-3 binding to GEF-H1, a microtubule-localized Rho exchange factor. *J. Biol. Chem.* **279**, 18392–18400 (2004).
62. MEEK, S. E., Lane, W. S. & Piwnicka-Worms, H. Comprehensive proteomic analysis of interphase and mitotic 14-3-3-binding proteins. *J. Biol. Chem.* **279**, 32046–32054 (2004).
63. Chen, X. & Macara, I. G. Par-3 mediates the inhibition of LIM kinase 2 to regulate cofilin phosphorylation and tight junction assembly. *J. Cell Biol.* **172**, 671–678 (2006).
64. Kligys, K. *et al.* The slingshot family of phosphatases mediates Rac1 regulation of cofilin phosphorylation, laminin-332 organization, and motility behavior of keratinocytes. *J. Biol. Chem.* **282**, 32520–32528 (2007).
65. Rollason, R., Korolchuk, V., Hamilton, C., Jepson, M. & Banting, G. A CD317/tetherin-RICH2 complex plays a critical role in the organization of the subapical actin cytoskeleton in polarized epithelial cells. *J. Cell Biol.* **184**, 721–736 (2009).
66. Torkko, J. M., Manninen, A., Schuck, S. & Simons, K. Depletion of apical transport proteins perturbs epithelial cyst formation and ciliogenesis. *J. Cell Sci.* **121**, 1193–1203 (2008).
67. Desclozeaux, M. *et al.* Active Rab11 and functional recycling endosome are required for E-cadherin trafficking and lumen formation during epithelial morphogenesis. *Am. J. Physiol. Cell Physiol.* **295**, C545–C556 (2008).
68. Cao, J., Albertson, R., Riggs, B., Field, C. M. & Sullivan, W. Nuf, a Rab11 effector, maintains cytokinetic furrow integrity by promoting local actin polymerization. *J. Cell Biol.* **182**, 301–313 (2008).
69. Schuh, M. An actin-dependent mechanism for long-range vesicle transport. *Nat. Cell Biol.* **13**, 1431–1436 (2011).
70. Rodal, A. A., Motola-Barnes, R. N. & Littleton, J. T. Nervous wreck and Cdc42 cooperate to regulate endocytic actin assembly during synaptic growth. *J. Neurosci.* **28**, 8316–8325 (2008).

METHODS

Nematode strains. Worm cultures and genetic crosses were carried out according to standard protocols⁷¹. The expression plasmids used to generate intestine-specific marker strains were based on the pAZ110 tagging plasmid backbone⁷² in which we introduced a ~3 kb sequence of the *pept-1* promoter derived from the pKN111 plasmid provided by Keith Nehrke³⁰. In the multiple cloning site following the promoter we inserted a coding sequence for an amino- or carboxy-terminal fluorescent protein tag such as GFP (derived from pPD95.79, A. Fire plasmids) or DsRed (amplified from pDsRed-N1, Clontech), as well as a PCR-amplified, genomic coding sequence of an organelle or membrane marker. All transgene insertions were created by biolistic transformation of *unc-119* mutant worms (DP38 (*unc-119(ed3)* III); ref. 72). To increase RNAi sensitivity, some single transgenic strains were crossed into the *rff-3* deficient strain NL2099 (*rff-3(pk1426)* II; ref. 73) provided by the Caenorhabditis Genetic Center (CGC), which is funded by the US National Institutes of Health (NIH) National Centre for Research Resources.

The double transgenic, primary screening strain MZE1 (*unc-119(ed3)* III; *cbgIs91[pPept-1::pept-1::DsRed;unc-119(+)]*; *cbgIs98[pPept-1::GFP::rab-11.1;unc-119(+)]*) resulted from the crossing of two marker strains, MZE91R expressing PEPT-1::DsRed (which in addition carries a deletion for *rff-3*) (*unc-119(ed3)* III; *cbgIs91[pPept-1::pept-1::DsRed;unc-119(+)]*; *rff-3(pk1426)* II) and MZE98 expressing GFP::RAB-11 (*unc-119(ed3)* III; *cbgIs98[pPept-1::GFP::rab-11.1;unc-119(+)]*). The double transgenic strains for secondary assay analysis resulted from crossing MZE91R with other GFP-organellar marker strains generated according to the description above or provided by the CGC. The secondary assay strains are MZE2 (*unc-119(ed3)* III; *cbgIs91[pPept-1::pept-1::DsRed;unc-119(+)]*; *cbgIs99[pPept-1::GFP::rab-5;unc-119(+)]*), MZE3 (*unc-119(ed3)* III; *cbgIs91[pPept-1::pept-1::DsRed;unc-119(+)]*; *cbgIs100[pPept-1::amans-2::GFP;unc-119(+)]*), MZE4 (*unc-119(ed3)* III; *cbgIs91[pPept-1::pept-1::DsRed;unc-119(+)]*; *cbgIs103[pPept-1::SP12::GFP;unc-119(+)]*) (AMANS-2::GFP and SP-12::GFP constructs were derived from plasmids provided by M. Rolls; ref. 74; Harvard Medical School) and MZE 5 (*unc-119(ed3)* III; *cbgIs91[pPept-1::pept-1::DsRed;unc-119(+)]*; *pwIs50[lmp-1::GFP + Cb-unc-119(+)]*). The original LMP-1::GFP-expressing RT25 strain⁷⁵ used to generate MZE5 was provided by the CGC.

The *rff-3* deficient, GFP::RAB-11-expressing strain MZE98R (*unc-119(ed3)* III; *cbgIs98[pPept-1::GFP::rab-11.1;unc-119(+)]*; *rff-3(pk1426)* II) was used for total worm protein extracts on single or double RNAi with *par-5*, and for immunofluorescence. The *fit-2*-deletion strain MT14355 (*fit-2(n4426)* X; ref. 76) was obtained from the CGC (deletion confirmed by PCR). MZE6 (*unc-119(ed3)* III; *cbgIs98[pPept-1::GFP::rab-11.1;unc-119(+)]*; *hum-2(ok596)*) results from crossing MZE98R and RB801, a *hum-2*-deletion strain provided by the CGC (deletion confirmed by PCR). The PGP-1::GFP strain was provided by K. Sato⁷⁷ (Gunma University). The RT348 strain expressing GFP::RME-1 was provided by B. Grant⁷⁵ (Rutgers University). The GFP::CDC-42-expressing strain TH51 (3-9) (*unc-119(ed3)* III; *ddEx14[pie-1p::GFP::R07G3.1(genomic);unc-119(+)]*) was provided by the Hyman laboratory (Max Planck Institute of Molecular Cell Biology and Genetics, MPI-CBG).

Feeding clones for RNAi. The genome-wide RNAi screen was carried out by the feeding method described previously⁷⁸ using the Ahringer feeding library⁷⁹ provided by Source BioScience LifeSciences UK Limited with 16,757 transformed *Escherichia coli* clones (strain HT115). The clone-set used for the *emb* screen comprised 1,037 selected feeding clones of this RNAi feeding library and was provided by T. Hyman (MPI-CBG). The *unc-60a/b* feeding clone was a gift from Carrie Cowan (Research Institute of Molecular Pathology, Vienna). The negative control for RNAi was an HT115 feeding clone transformed with L4440 vector encoding for scrambled dsRNA without a corresponding target in the worm genome (referred to as feeding control). Self-cloned RNAi constructs using the L4440 feeding vector include F07F6.4 (the positive RNAi control in the primary screen), *ced-10/rac1*, *rho-1* (two constructs) and *nud-2*. Generally, we subcloned ~1 kilobase (kb) of genomic DNA consisting mostly of exons into L4440 using the following primers: F07F6.4-FW-Bgl-II 5'-CATAGATCGAAATCTTCTCTCT-3'; F07F6.4-REV-Hind-III 5'-CATAAGCTTCTCCATTTGCTTTC-3'; *ced-10*-FW-NheI 5'-GAGCCTAGCGTATTGACAACACTACTCAGCAAATG-3'; *ced-10*-REV-XmaI 5'-GACCCGGGCATCTAGACACCGTACTACTTG-3'; *rho-1*-FW1-NheI 5'-GACGCTAGCCACATAGATAGATAGTGGTCGC-3'; *rho-1*-REV1-XmaI 5'-GACCCGGGCACAAATTTCTTCATCAATCCGC-3'; *rho-1*-FW2-NheI 5'-GACGCTAGCTCTGACGTCGAACCTGCTCTATG-3'; *rho-1*-REV2-XmaI 5'-GACCCGGGCATCTCTCAATTCGGTCTACTGC-3'; *nud-2* FW-NheI 5'-GACGCTAGCGATCGACAGGACGATTCCCGTG-3'; *nud-2* REV-XmaI 5'-GACCCGGGGTTAAGCCCGTGTCGTTGTAAGATG-3'.

PCR validation of bacterial clones. To confirm the sequence of identified RNAi clones from the feeding library⁷⁹, we isolated the L4440 plasmid DNA and sequenced its dsRNA coding region with a forward (5'-GACCGAGCGACGAGTCAGTG-3') or reverse (5'-CACTGGCCGTCGTTTTACAAC-3') sequencing primer.

Single- and double-RNAi feeding experiments. Single bacterial clones were inoculated in 4 ml Luria broth (LB) medium (plus 100 µg ml⁻¹ ampicillin (Amp) and 5 µg ml⁻¹ tetracycline (Tet)), grown for 8 h to overnight at 200 r.p.m., and the bacteria pelleted and resuspended in ≤500 µl NGM+ (nematode growth medium containing 100 µg ml⁻¹ Amp, 5 µg ml⁻¹ Tet and 1 mM isopropyl-β-D-thiogalactoside) of which ≤150 µl were seeded on 6 cm NGM+ plates. Seeded plates were dried under an airflow hood and induced in the dark for 8 h to overnight at room temperature. For double-RNAi experiments with *par-5*, we chose a feeding clone ratio of 1:3 (one part (*par-5*) plus two parts (second gene x)). Applied to the reference sample (*par-5* + FC), this 1:3 ratio resulted in a *par-5* RNAi phenotype frequency of ~50%, which enabled detection of suppression as well as exacerbation of the *par-5* RNAi phenotype on double RNAi. The feeding clones were inoculated in an overnight culture of 20 ml (*par-5*) or 5 ml (clone x) LB medium (plus 100 µg ml⁻¹ Amp and 5 µg ml⁻¹ Tet). The bacteria were pelleted and resuspended in 2.5 ml (*par-5*) or 0.4 ml (clone x) NMG+ medium. For OD₆₀₀ measurements, these resuspended bacteria were diluted 1:80 in 1 ml NGM+ medium. The OD₆₀₀ ratio of *par-5* to clone x was determined and used to calculate the 'volume x' of clone x for a 1:3 mixture with the *par-5* bacteria (one part (50 µl *par-5* bacteria) plus two parts (OD₆₀₀-corrected 'volume x' of 'clone x' bacteria)). These volumes were multiplied by the number of feeding plates used per double-RNAi sample, that is at least by two. Per 6 cm NGM+ feeding plate, ≤150 µl of the final 1:3 double-RNAi mixture was seeded. One plate or half of the plates of each sample with adult, double-RNAi-treated worms was used to produce total worm protein extracts to confirm similar levels of PAR-5 depletion by western blot (Fig. 6a and Supplementary Fig. S8b,c). The other plate or half of the plates was examined by epifluorescence microscopy to determine the *par-5* RNAi phenotype frequency, that is the mean percentages of intestines with one or more peripheral GFP::RAB-11 recycling endosome clusters.

Immunofluorescence stainings on dissected intestines. Approximately 30–40 young adult worms were picked and transferred to a 10 µl droplet of cutting buffer (1×M9 or 1×PBS buffer containing 0.001% Tween-20 + 0.25 mM levamisole ((-)-tetramisole hydrochloride, Sigma-Aldrich) on a coverslip for decapitation. Dissected worms were transferred from cutting buffer into a 0.2 ml Thermotube ('PCR tube', a thin-walled tube with flat or domed cap, ABgene), left to settle by gravity or spun down in a microcentrifuge (2,000g, 30 s) and the buffer exchanged for fixation buffer (either 1.25–4% freshly diluted paraformaldehyde (PFA) (in 1×PBS, 0.001% Tween-20) for subsequent F-actin staining with fluorescent phalloidins, or ice-cold 100% methanol (containing 0.001% Tween-20)) to fix the samples for 10–15 min at room temperature or 5 min on dry ice, respectively. Methanol fixation of dissected worms was preferentially used for all primary antibodies except anti-CASP, which gave better staining results on PFA fixation. PFA fixation, which is obligatory for fluorescent phalloidin staining of F-actin, diminished the apical enrichment of GFP::RAB-11-labelled recycling endosomes.

After PFA fixation, samples were either permeabilized for 10 min in 1×PBS + 0.1% Tween-20 (for some antibodies with 0.01% Tween-20 or Triton X-100), or directly blocked in blocking solution (1×PBS, 0.001% Tween-20, 2% BSA) on a rotor wheel for 1 h with three buffer changes. Post blocking, samples were incubated overnight at 4 °C on a rotor wheel with primary antibody diluted in blocking buffer (1×PBS, 0.001–0.01% Tween-20, 2% BSA; 50–100 µl added per PCR tube).

Primary antibodies for immunofluorescence and dilutions: anti-CASP (1:2,000) (gift from Sean Munro, Cambridge; ref. 80); anti-ERM-1 (1:200) (gift from Olaf Bossinger, Rheinisch-Westfälische Technische Hochschule Aachen; ref. 81); anti-RAB-11 and anti-RAB-5 (1:500–1:1,000) (gift from Anne Spang, University of Basel; ref. 82); MH33 (anti-IFB-2, 1:100) and MH27 (anti-AJM-1, 1:500) (the monoclonal antibodies MH33 and MH27 developed by R. H. Waterstone were obtained from the Developmental Studies Hybridoma Bank developed under the auspices of the US National Institute of Child Health and Human Development and maintained by the University of Iowa, Department of Biology); anti-α-tubulin (clone DM1A, 1:500, Sigma-Aldrich), anti-γ-tubulin (1:30,000; ref. 83); anti-EPS-8 (1:50) (gift from Pier Paolo Di Fiore, Italian FIRC Institute of Molecular Oncology–European Institute of Oncology Campus, Milan, Italy; ref. 84); anti-PKC-3 (1:1,000, PKC ζ (C-20) sc-216, Santa Cruz Biotechnology). Anti-PAR-6 (1:5,000) and anti-PAR-3 (serum 1:1,500–1:3,000) were gifts from T. Hyman (MPI-CBG; both described in ref. 85).

Before addition of the secondary antibodies, samples were washed 3 × 20 min at room temperature in washing buffer (1×PBS, 0.001–0.01% Tween-20). Alexa Fluor conjugated secondary antibodies (Alexa Fluor 405/488/555/647 goat anti-mouse or goat anti-rabbit IgG (H + L), Molecular Probes) were diluted 1:500 in blocking solution and PCR tubes were incubated for 2 h at room temperature on a rotor wheel, followed by 3 × 20 min washes at room temperature. For staining of F-actin with fluorescent phalloidin (rhodamine phalloidin (Cytoskeleton) or Alexa Fluor 488 phalloidin (Molecular Probes)), this was diluted 1:140 in 1×PBS + 0.001% Tween-20 and applied during secondary antibody incubation or after PFA fixation for 1–1.5 h in the dark. After washing 3 × 20 min, dissected worms were left to settle, the supernatant removed and the worms transferred with 10–20 µl Vectashield (Vector Labs) to coverslips. The coverslips were adhered with 2% agarose pads and sealed with nail polish.

Antibodies for western blot analysis and confirmation of RNAi efficiency.

Western blot analysis was carried out with total worm protein extracts after separation by SDS-PAGE. RNAi-treated, young adult worms were removed from feeding plates either by picking 50 worms or by washing off the plate with 0.5–1 ml 1×M9 buffer +0.001% or 0.01% Tween-20, transferred to 1 ml reaction tubes, left to settle for 5 min on ice by gravity or centrifuged for 1 min at 400g, and washed two or three times to remove bacteria. The volume over the settled worms was reduced to 20 or 40 µl (marked on the tube), supplemented with Laemmli buffer, put at 95 °C for 2 min, sonicated for 10 min, put at 95 °C for 2 min and centrifuged at 20,000g for 10 min to pellet residual debris before loading. Antibodies used for western blot probing included anti-PAR-5 antibodies (gifts from Andy Golden⁴² (US National Institute of Diabetes and Digestive and Kidney Diseases) and T. Hyman⁸⁵ (MPI-CBG), 1:3,000 and 1:5,000, respectively), mouse anti-actin (clone C4; Chemicon, Millipore) used at 1:40,000 and anti-RHO-1 (ref. 86; gift from T. Hyman (MPI-CBG)). For CDC-42, RAC-1 and PAR-3, no suitable antibodies for western blot probing were available. Therefore, *cdc-42* RNAi efficiency was assessed by means of the GFP::CDC-42-expressing strain TH51 (gift from T. Hyman (MPI-CBG)) and anti-GFP probing (antibody generated in house by David Drechsel (MPI-CBG); Supplementary Fig. S8c). Efficient *rac-1* RNAi correlated with reduced GFP::RAB-11 fluorescence intensities (our unpublished observations). Efficient PAR-3 depletion correlated with previously described phenotypes, that is perturbed germline morphologies and egg laying defects (judged by differential interference contrast microscopy). Furthermore, AJM-1 staining revealed perturbed spermatheca morphology in PAR-3-depleted worms, in line with previous reports⁸⁷.

Confocal laser scanning microscopy of worms during secondary assays and *par-5* RNAi phenotype analysis.

Approximately ~30 live RNAi-treated worms were collected manually from feeding plates, paralysed in 10 mM levamisole and mounted on a 2% agarose pad. Fluorescent images were obtained using a Zeiss LSM Meta or Zeiss LSM DuoScan microscope (Carl Zeiss MicroImaging) with a ×63 numerical aperture 1.4 Oil Plan-Apochromat objective or a ×40 numerical aperture 0.45 water emulsion Plan-Apochromat objective with a differential interference contrast prism, respectively. Signals after excitation with 405 nm and band-pass 420–480 filter emission were used to identify broad-spectrum LRO autofluorescence. DsRed and GFP signals were recorded in a sequential manner by frame or line-scan. DsRed was excited before GFP at 543 nm (LSM Meta) or 561 nm (LSM DuoScan) and emission collected with band-pass 585–615 (LSM Meta) or long-pass 575 (LSM DuoScan) filters. GFP signals were measured with 488 nm excitation and band-pass 505–530 emission filters. Imaging settings were adjusted for each sample to avoid pixel saturation. The settings were carefully tested with single and double transgenic lines to exclude bleed-through events between GFP and DsRed. Only DsRed or GFP signals that did not correlate with autofluorescence signals were considered as specific. Images were processed and analysed using Fiji (<http://fiji.sc/wiki/index.php/Fiji>), an image-processing package based on NIH ImageJ. If indicated, brightness and contrast were adjusted for better visibility using Photoshop (Adobe Systems).

Epifluorescence microscopy in secondary assays and *par-5* RNAi analysis.

To analyse selected RNAi clones for LRO phenotypes, we used the epifluorescent Axio Imager Z1 microscope (Carl Zeiss MicroImaging; filter set, excitation 365 nm, beam splitter FT 395, emission band-pass 445/50). The *par-5* RNAi phenotype frequency on double RNAi was validated by counting phenotypic worms with one or more GFP::RAB-11-labelled recycling endosome cluster per intestine and determination of the percentage of phenotypic worms per sample. Worms from each double-RNAi feeding plate sample were washed three times in 1×M9 (+0.01% Tween-20), resuspended in 250 µl, of which 120 µl was transferred into separate wells on a 'µ-Slide 8 well' (ibiTreat, ibidi). Before phenotypic analysis, live worms were paralysed by adding 30 µl 100 mM sodium azide (yielding 20 mM final NaN₃) to prevent twitching. Wild type and *par-5* phenotypic worms were counted manually using the Zeiss Axiovert 200M (Carl Zeiss MicroImaging), an inverted wide-field microscope, equipped with a SPOT RT camera (Diagnostic Instruments) and fitted with a Zeiss Plan-Apochromat ×10 numerical aperture 0.45 objective. For analysis of rhodamine phalloidin-stained F-actin, the Zeiss EC Plan-Neofluar ×40 numerical aperture 0.75 objective was used.

Intensity profile extraction. To compute the ectopic:apical intensity ratios of rhodamine phalloidin-stained F-actin and GFP::RAB-11 in control, *par-5* and *arp-1* RNAi-treated intestines, we collected intensity profiles along 20-pixel-wide lines drawn perpendicularly to the worm intestines in Fiji (<http://fiji.sc/wiki/index.php/Fiji>). Both actin and GFP::RAB-11 intensity profiles were measured on the same line. Each profile contains a set of (x_i, y_i) couples, indicating the position along the line and the associated intensity value. To assess differences in the mean peripheral (ectopic) and apical F-actin or GFP intensities, we acquired the line-based intensity profiles (or 'intensity profiles') only at sites where the peripheral patches were seen at the outmost margin of the enterocytes or intestine and optically well separated from the actin-rich apical domain. Furthermore, regions with more out-of-focus

light or close-by, overly bright tissues (such as pharynx or muscles) were excluded. Intensity profiles were acquired with the same criteria in control intestines lacking ectopic patches and peripherally clustered recycling endosomes.

Intensity profile quantification. The same procedure was applied for both F-actin and GFP::RAB-11 intensity quantification (implemented in MATLAB, MathWorks). Intensity profiles were first normalized to the same unit length along the x axis, to compensate for different intestinal widths, and then equalized along the y axis through baseline subtraction, to correct for different background intensities. A median filter was carried out on the normalized curves and peaks were detected with a peak detection algorithm in three different regions: from left and right each 25% covering the 'basal' (or ectopic) parts of the profile, and 50% covering the central, apical part of the profile. Peaks were identified as local maxima in one of these three areas of the smoothed normalized profile. We subsequently manually controlled the correct assignment of apical versus ectopic peaks. Peak identification enabled the extraction of quantitative features such as position, intensity and ectopic:apical intensity ratios. Peak position indicates the relative position of each peak on the x axis (intestinal width); peak intensity indicates the absolute marker intensity; the intensity ratio indicates the ratio of intensity in the basal, ectopic peaks to the central, apical ones. To determine the width and intensity of each peak in a robust way, we fitted them with a peak fitting procedure based on Gaussian fitting. The extracted values were then averaged and compared across the different knockdown conditions to quantify apical and basal mean peak intensities, and their ratio.

Total actin quantification. The total amount of F-actin was assessed through region-of-interest-based quantification on rhodamine phalloidin-stained intestines of selected control and *par-5* RNAi-treated, phenotypic animals. The area of approximately two to three segments of each imaged intestine considered for the intensity profile analysis was traced, and the mean actin intensity determined using Fiji software (<http://fiji.sc/wiki/index.php/Fiji>). Out-of-focus areas and areas close to overly exposed tissues were excluded from analysis.

Statistical analysis. The statistical significance of intensity measures (Fig. 4d,f,g) and phenotype frequencies (Fig. 6b) was assessed with Wilcoxon rank sum tests. The significance of functional enrichments in the hit set (Fig. 2c) was assessed with the hypergeometric distribution. Results are expressed as mean ± s.e.m.

71. Brenner, S. The genetics of *Caenorhabditis elegans*. *Genetics* **77**, 71–94 (1974).
72. Praitis, V., Casey, E., Collar, D. & Austin, J. Creation of low-copy integrated transgenic lines in *Caenorhabditis elegans*. *Genetics* **157**, 1217–1226 (2001).
73. Simmer, F. *et al.* Genome-wide RNAi of *C. elegans* using the hypersensitive *rrf-3* strain reveals novel gene functions. *PLoS Biol.* **1**, E12 (2003).
74. Rolls, M. M., Hall, D. H., Victor, M., Stelzer, E. H. & Rapoport, T. A. Targeting of rough endoplasmic reticulum membrane proteins and ribosomes in invertebrate neurons. *Mol. Biol. Cell* **13**, 1778–1791 (2002).
75. Chen, C. C. *et al.* RAB-10 is required for endocytic recycling in the *Caenorhabditis elegans* intestine. *Mol. Biol. Cell* **17**, 1286–1297 (2006).
76. Berdichevsky, A., Viswanathan, M., Horvitz, H. R. & Guarente, L. *C. elegans* SIR-2.1 interacts with 14-3-3 proteins to activate DAF-16 and extend life span. *Cell* **125**, 1165–1177 (2006).
77. Sato, T. *et al.* The Rab8 GTPase regulates apical protein localization in intestinal cells. *Nature* **448**, 366–369 (2007).
78. Timmons, L., Court, D. L. & Fire, A. Ingestion of bacterially expressed dsRNAs can produce specific and potent genetic interference in *Caenorhabditis elegans*. *Gene* **263**, 103–112 (2001).
79. Kamath, R. S. & Ahringer, J. Genome-wide RNAi screening in *Caenorhabditis elegans*. *Methods* **30**, 313–321 (2003).
80. Gillingham, A. K., Pfeifer, A. C. & Munro, S. CASP, the alternatively spliced product of the gene encoding the CCAAT-displacement protein transcription factor, is a Golgi membrane protein related to giantin. *Mol. Biol. Cell* **13**, 3761–3774 (2002).
81. Van Fürden, D., Johnson, K., Segbert, C. & Bossinger, O. The *C. elegans* ezrin–radixin–moesin protein ERM-1 is necessary for apical junction remodelling and tubulogenesis in the intestine. *Dev. Biol.* **272**, 262–276 (2004).
82. Poteryaev, D., Fares, H., Bowerman, B. & Spang, A. *Caenorhabditis elegans* SAND-1 is essential for RAB-7 function in endosomal traffic. *EMBO J.* **26**, 301–312 (2007).
83. Hannak, E., Kirkham, M., Hyman, A. A. & Oegema, K. Aurora-A kinase is required for centrosome maturation in *Caenorhabditis elegans*. *J. Cell Biol.* **155**, 1109–1116 (2001).
84. Croce, A. *et al.* A novel actin barbed-end-capping activity in EPS-8 regulates apical morphogenesis in intestinal cells of *Caenorhabditis elegans*. *Nat. Cell Biol.* **6**, 1173 (2004).
85. Hoegge, C. *et al.* LGL can partition the cortex of one-cell *Caenorhabditis elegans* embryos into two domains. *Curr. Biol.* **20**, 1296–1303 (2010).
86. Schonegg, S. & Hyman, A. A. CDC-42 and RHO-1 coordinate actomyosin contractility and PAR protein localization during polarity establishment in *C. elegans* embryos. *Development* **133**, 3507–3516 (2006).
87. Aono, S., Legouis, R., Hoose, W. & Kempheus, K. PAR-3 is required for epithelial cell polarity in the distal spermatheca of *C. elegans*. *Development* **131**, 2865–2874 (2004).

Correction notice

Nature Cell Biology (2012) | doi:10.1038/ncb2508

***Caenorhabditis elegans* screen reveals role of PAR-5 in RAB-11-recycling endosome positioning and apicobasal cell polarity**

Julia Franziska Winter, Sebastian Höpfner, Kerstin Korn, Benjamin O. Farnung, Charles R. Bradshaw, Giovanni Marsico, Michael Volkmer, Bianca Habermann & Marino Zerial

In the version of this Article initially published online, PEPT-2::DsRed should have been PEPT-1::DsRed in Supplementary Fig. S1d. In Supplementary Fig. 3e, some text elements in the column for gene annotations were erroneous or lost. The legend for Supplementary Fig. S6 should have referred to α -tubulin rather than β -tubulin. These errors have been corrected.

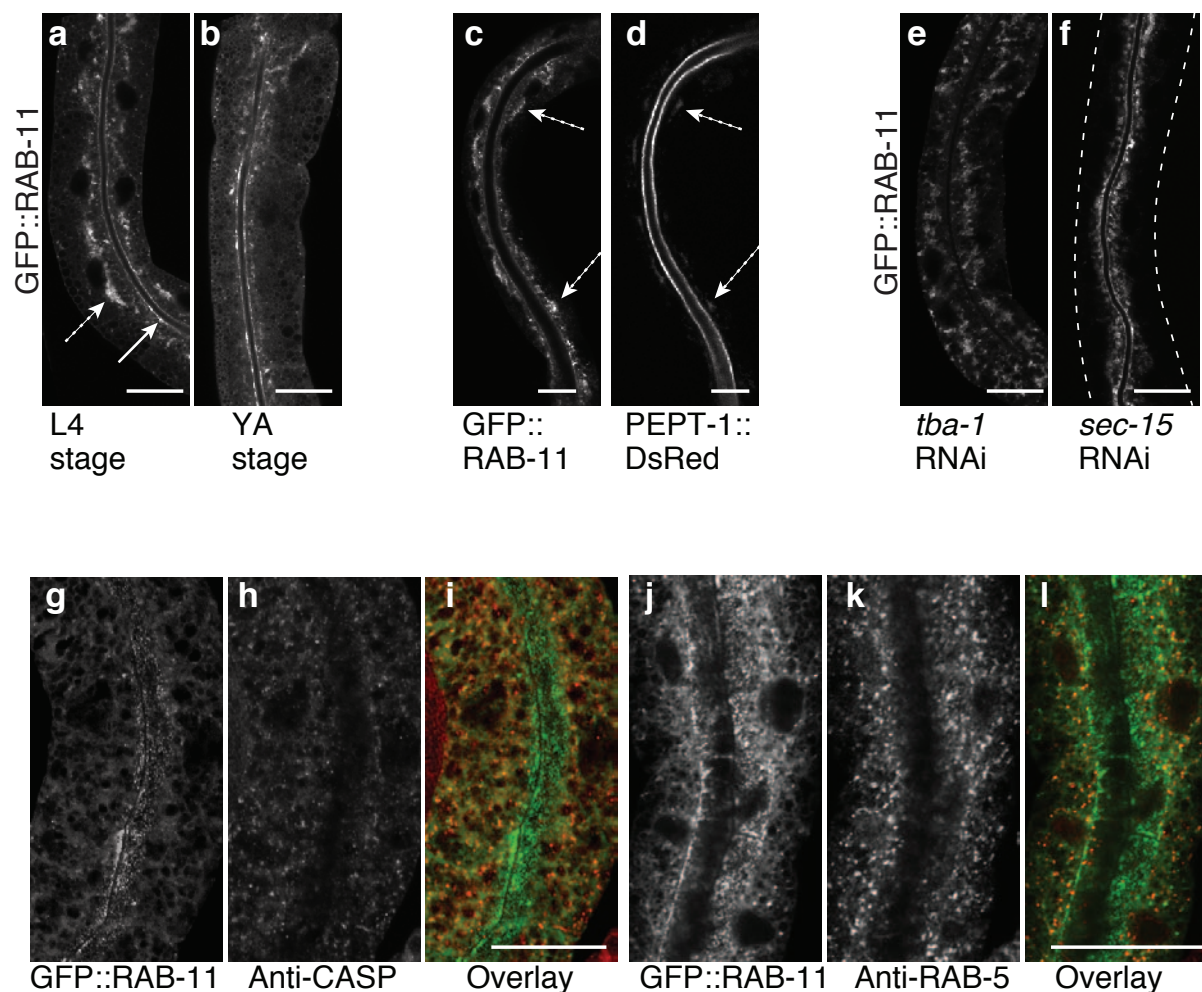


Figure S1 GFP::RAB-11 labelled endosomes share characteristics with Rab11-endosomes of higher metazoan epithelia. (a-f) Confocal images of L4 to young adult (YA) stage worms of the screening strain. (a,b) In L4 stage animals, GFP::RAB-11 labels REs enriched along the apical domain (arrow in a) as well as bulkier organelles that enrich subapically (dashed arrow in a) and become less apparent in YA stage animals (b). (c, d) Fractions of the apical membrane protein PEPT-1::DsRed can be observed in the subapical, bulkier GFP::RAB-11 positive REs (dashed arrows). This accounts for on average 20% (n=11/54) of L4 to YA-stage MZE1 worms. For endogenous RAB-11 labelled REs see Supplementary Information, Fig. S5a online. (e) Depletion of α -tubulin abrogates apical enrichment, and GFP::RAB-11-REs scatter. (f) Depletion of SEC-15, a Rab11-effector and component of the exocyst complex implicated in basolateral vesicle transport and tethering,

increases the apical enrichment of GFP::RAB-11-REs. (g-l) GFP::RAB-11 expressing intestines immunostained for CASP (g-i), or RAB-5 (j-l) to visualise the distinct distribution of REs versus Golgi and early endosomes, respectively. GFP::RAB-11-REs tend to be more apically enriched than early endosomes, in particular when compared to Golgi bodies, which are more evenly distributed. Note that the endotube is not a round, but rather folded tubing that can alternate along the vertical and longitudinal axes of the intestine. Thus, depending on the angle of optical sectioning of the endotube, the gut lumen's width and endotube morphology can vary. The optical section in (g) cuts the endotube at the level of the enclosing apical membrane at which GFP::RAB-11-labelled REs accumulate. The optical section in (j-l) cuts a flatly folded endotube more centrally, showing parts of its lumen. Scale bars indicate 20 μ m.

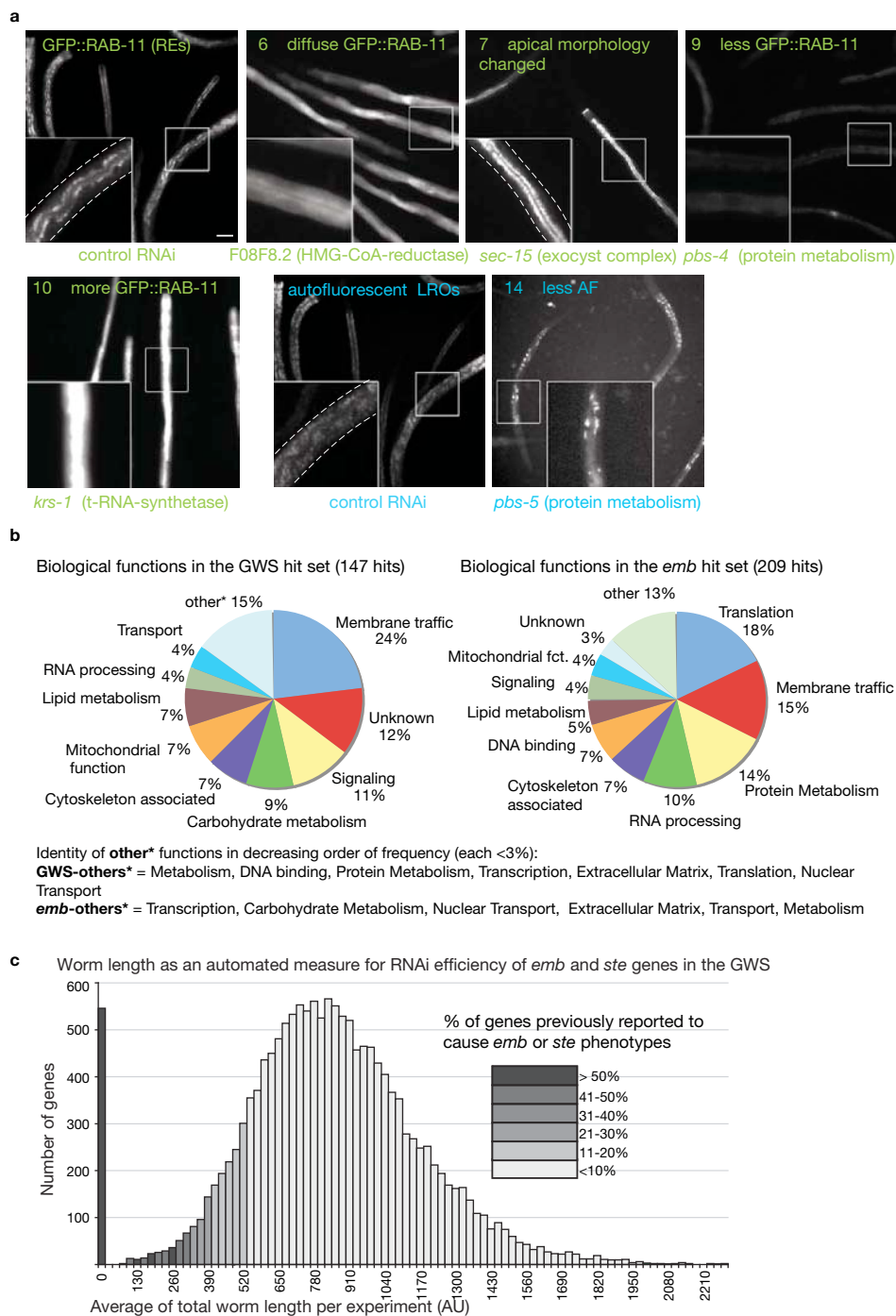


Figure S2 Remaining phenotypic defect categories, biological functions of primary screen hits, and automated assessment of RNAi efficiency in the GWS. (a) Complementary to Figure 2a: Remaining 5 of 14 phenotypic defect categories. For each phenotypic category, a representative image of a primary screen RNAi experiment is shown to indicate the characteristic changes of marker distribution or intensity compared to control RNAi. An altered morphology or distribution of apically enriched REs (category 7) is predominantly caused by exocyst complex components. The strongest increase or gain of RAB-11::GFP-intensity (category 10) is caused by depletion of genes encoding t-RNA-synthetases. Reduced fluorescence intensities for the individual markers (categories 9, 14) occur frequently upon depletion of genes required for protein metabolism. Scale bar in (a) is 50 μ m, and 20 μ m for the close-up. (b) Comparison of biological functions present in the individual hit sets obtained in the GWS (147 hits) and the

emb-screen (209 hits). Absolute contributions of biological functions to each hit set are shown. The GWS hit set comprises mostly 'membrane trafficking' genes (24%) and genes of yet unknown biological functions (in total 12%, of which 30% are conserved) with a potential role in epithelial membrane trafficking and cell polarity. The *emb*-screen hit set comprises more genes of core biological functions such as 'translation' and 'protein metabolism' that affect general biological processes. 'Membrane trafficking' is the second most abundant biological function (15%) in the *emb* hit set. (c) Worm length as an automated measure of RNAi efficiency in the GWS for *emb* and *ste* genes. The average total worm length per well was computed by automated image analysis for each RNAi experiment in the GWS. This measure results from the number of worms per well and their average length. Short worm length values occurred frequently upon RNAi of established *emb* or *ste* genes (acc. to WormBase release WS152).

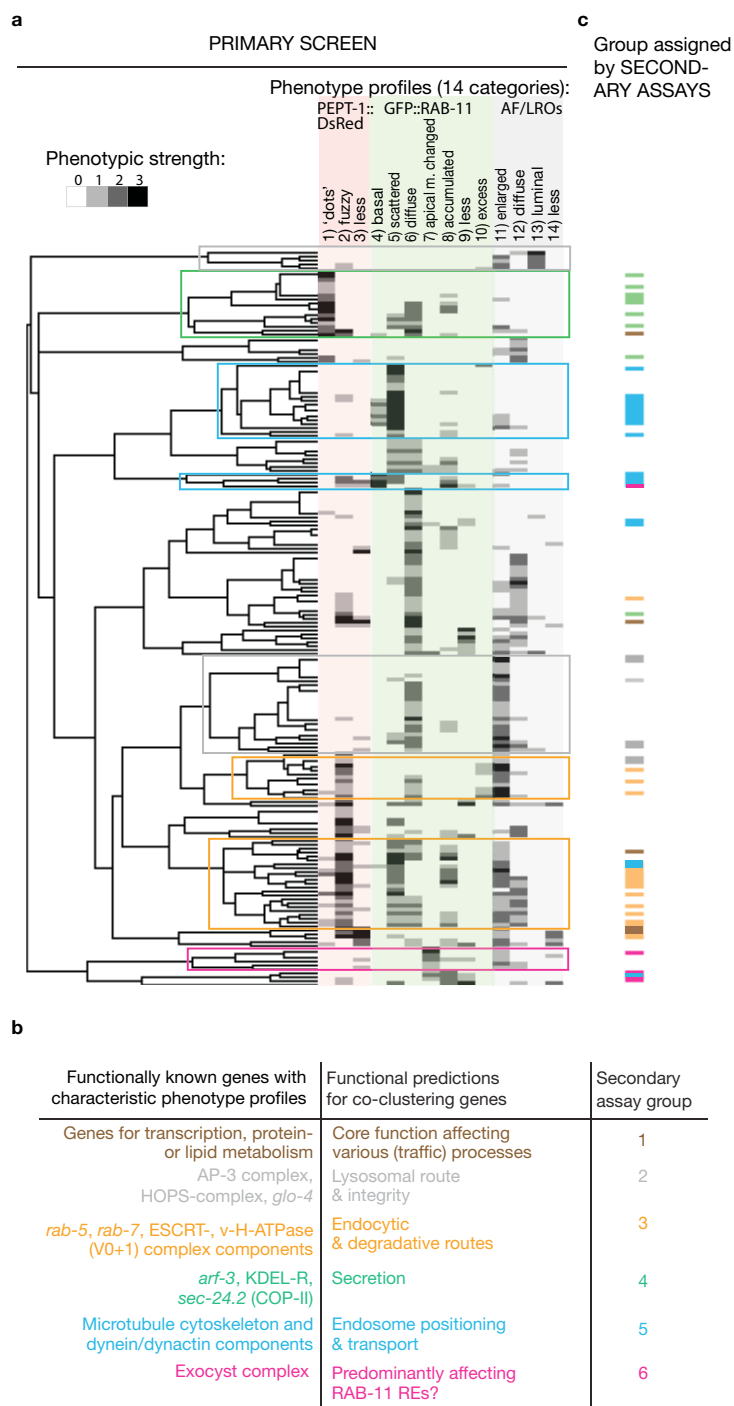


Figure S3 Hierarchical clustering reveals groups of genes with similar phenotype profiles and allows functional predictions for uncharacterised genes. **a-c** (a) Compact hierarchical clustering dendrogram of phenotype profiles of 189 primary-screen candidates, excluding all candidate genes implicated in biosynthesis and metabolism (such as 'translation' or 'protein metabolism', see Supplementary Information, Table S1 online). Phenotype strength ranges from 1 (weak, light grey) to 3 (strong, black). Along the x-axis of the dendrogram, the length of edges indicates the correlation between clusters. Coloured frames highlight clusters with functionally characteristic phenotype profiles upon RNAi of established trafficking regulators, e.g. gene implicated in secretion (green) and minus-end directed microtubule-based transport (blue), or degradation (orange). Functionally yet unknown,

co-clustering genes are predicted to exert a similar function. (b) Established traffic regulators selected from framed clusters (in a) with the inferred, functional predictions for co-clustering genes. (c) Following secondary assay analysis of 60 selected genes, these were assigned to one of the six groups as indicated by coloured bars. The matching colours of bars (c) and frames (a) indicate confirmed functional predictions. **d and e** Two hierarchical clustering dendrograms generated for the selected subset of 189 genes (d) and for the full set of 356 hits (e). The clustering dendrograms indicate for each candidate the gene name, biological function and the description either from NCBI KOG (K, version 090828), Wormbase (W, release WS204), or InterPro Domain (I, version 22.0) in that particular priority. The colour coding of the secondary assay groups corresponds to the colours used in Figure S3c.

Figure S3d: Hierarchical clustering of a subset of 189 primary HCS hits excluding genes with 'core' functions affecting all biological processes (specified in Table S1).

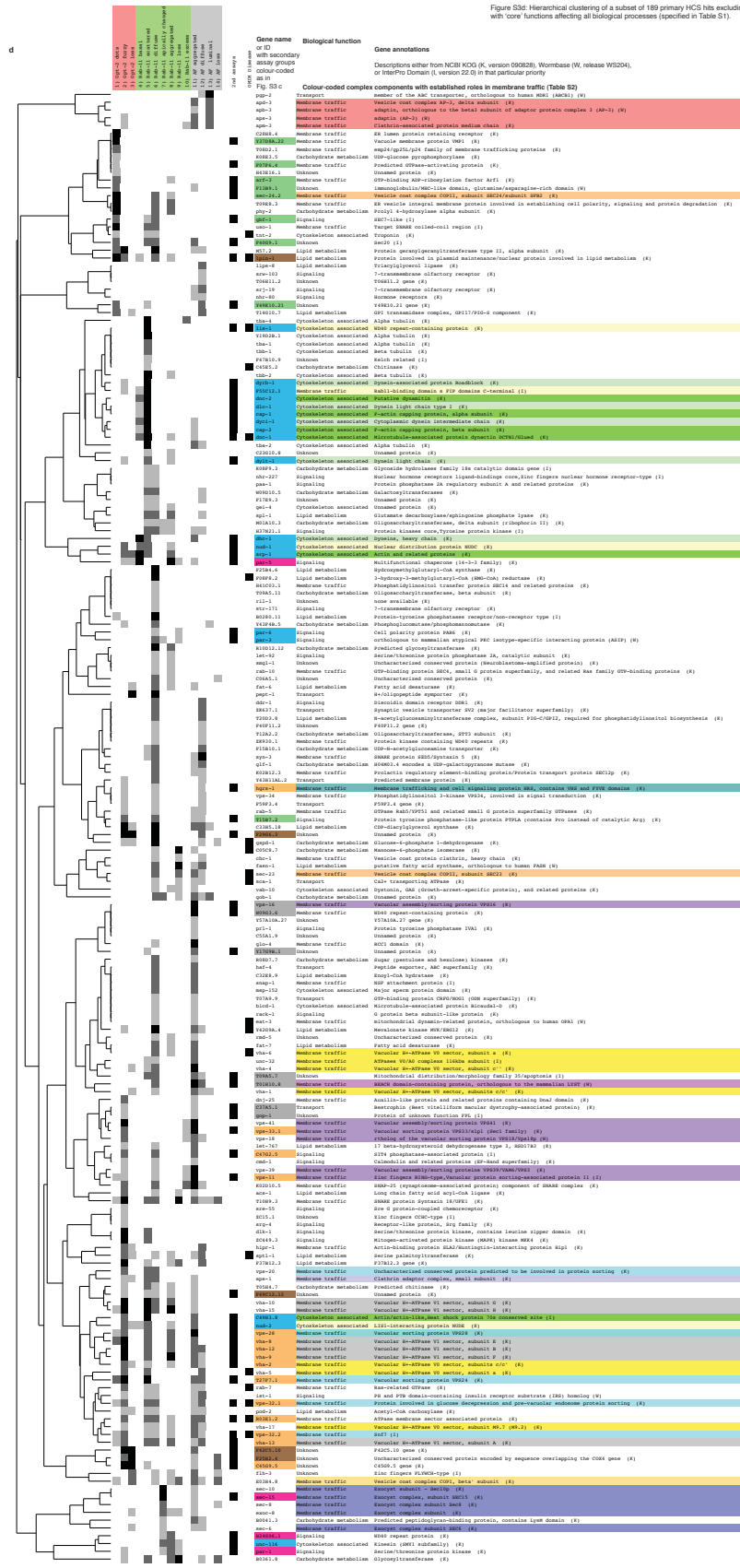


Figure S3 continued

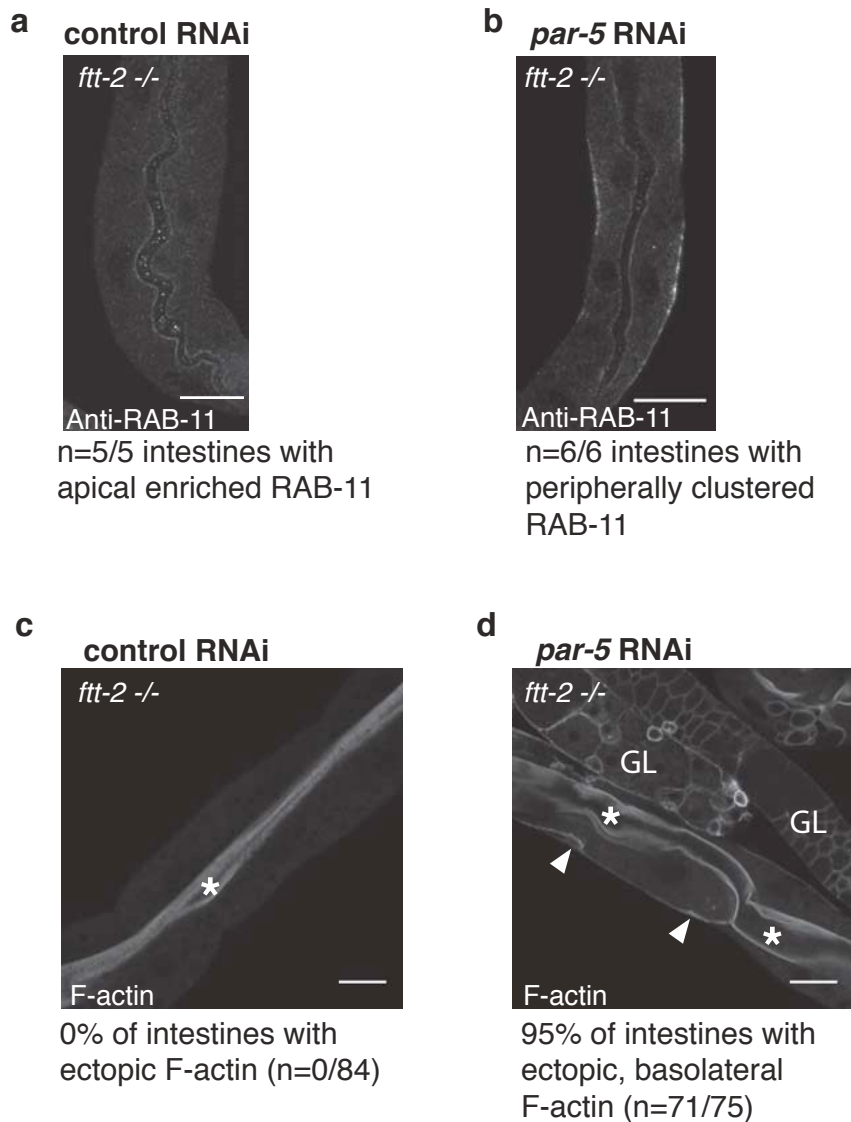


Figure S4 Ectopic F-actin upon PAR-5 (FTT-1) depletion as well as upon cofilin depletion interferes with RAB-11 RE positioning and causes clustering of RAB-11-REs. (a-d) PAR-5 (FTT-1), but not FTT-2, is required for RE-positioning and proper F-actin organisation. (a, b) Control RNAi intestines of the *ftt-2* deletion strain MT14355 exhibit apically enriched RAB-11-REs and normal apico-basal F-actin asymmetry. (c, d) *Par-5* RNAi causes RAB-11-RE-clustering and a frequent and strong F-actin phenotype in enterocytes and germlines (GL). Arrowheads mark ectopic, peripheral F-actin. Asterisks mark gut lumen. (e-l) Rhodamine phalloidin stained, RNAi treated intestines with GFP::RAB-11 labelled REs (e,f,i,j), or basal, GFP::RME-1 labelled REs (g,h,k,l). For improved visualisation, brightness and contrast were increased in the grey-scale images. (e-h) In control RNAi, F-actin concentrates at the apical domain (e,g, medial sections) and is barely detectable at the basolateral cortex (f,h, peripheral sections). (g,h) GFP::RME-1 labelled basal REs enrich basolaterally in control RNAi. (i-l) Upon PAR-5 depletion, GFP::RAB-11 labelled REs cluster peripherally around or closely to ectopic F-actin structures at the basolateral

cortex (i,j), whereas basal, GFP::RME-1 labelled REs do not cluster at ectopic F-actin sites but virtually disappear (k,l, n=10 intestines). (m-o) *Par-5* RNAi treated, non-transgenic intestines (NL2099 strain) show that ectopic F-actin (green) is more frequently and strongly surrounded or covered by endogenously labelled RAB-11-REs than by endogenous RAB-5-EEs (both in red, compare close-ups). (o) Mean percentage of all ectopic F-actin patches enriched for endogenously labelled RAB-11 or RAB-5 endosomes (analysed from n intestines with spatially well-defined ectopic F-actin patches, with n deriving from 2 independent experiments). Errorbars indicate s.e.m. and were derived using the m values. (p-s) Both RNAi of *par-5* and of *unc-60* (ADF-cofilin) cause ectopic microfilaments and clustered RAB-11-REs in enterocytes, but of different morphology and distributions. RAB-11-RE-clusters accumulate peripherally upon *par-5* RNAi (p,q), and more often apically upon *unc-60* RNAi (r,s). Brightness and contrast increased of peripheral grey-scale F-actin images of q and s. The scale bar indicates 10µm in the grey-scale images of m,n, as well as in p-s, and 20µm in all other images.

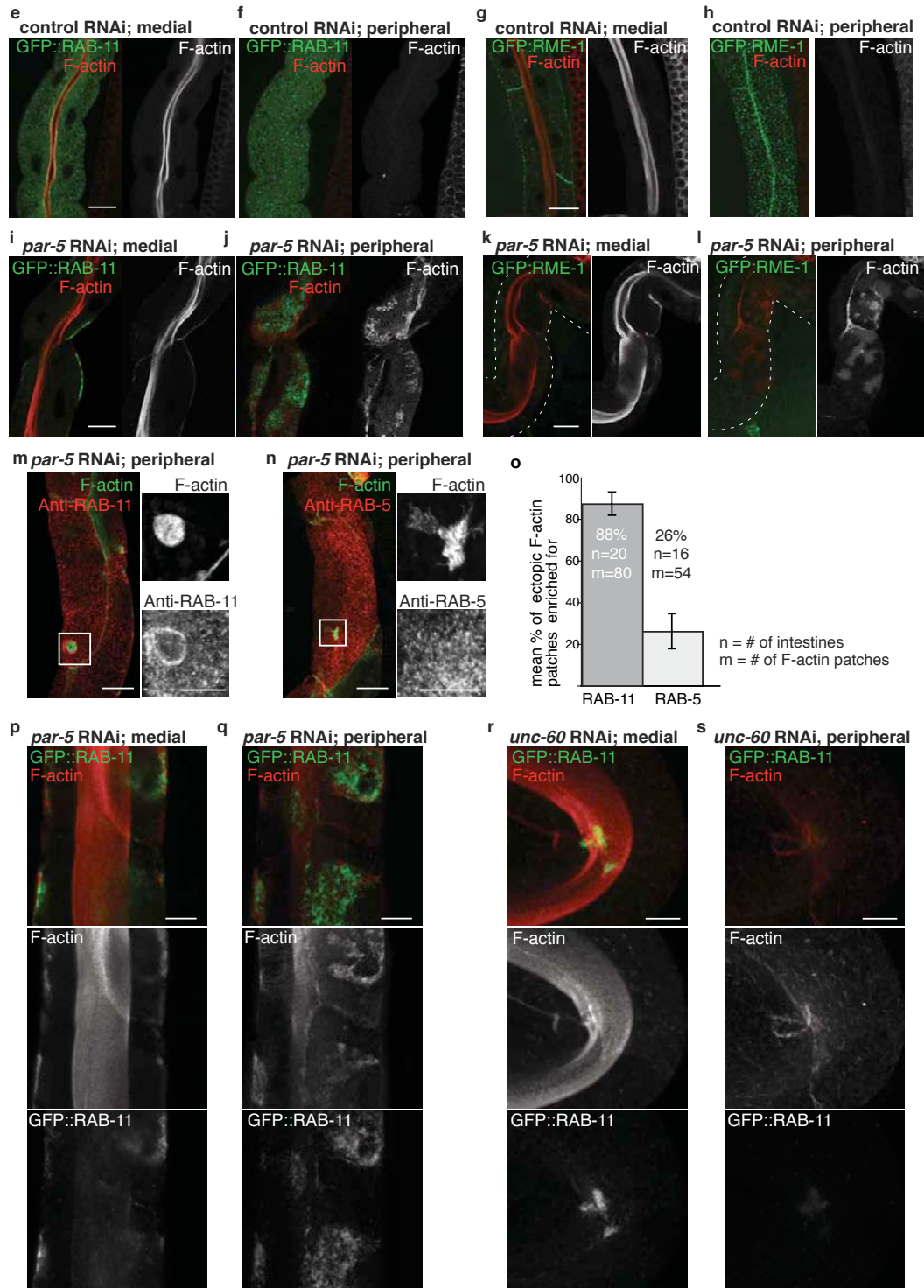


Figure S4 continued

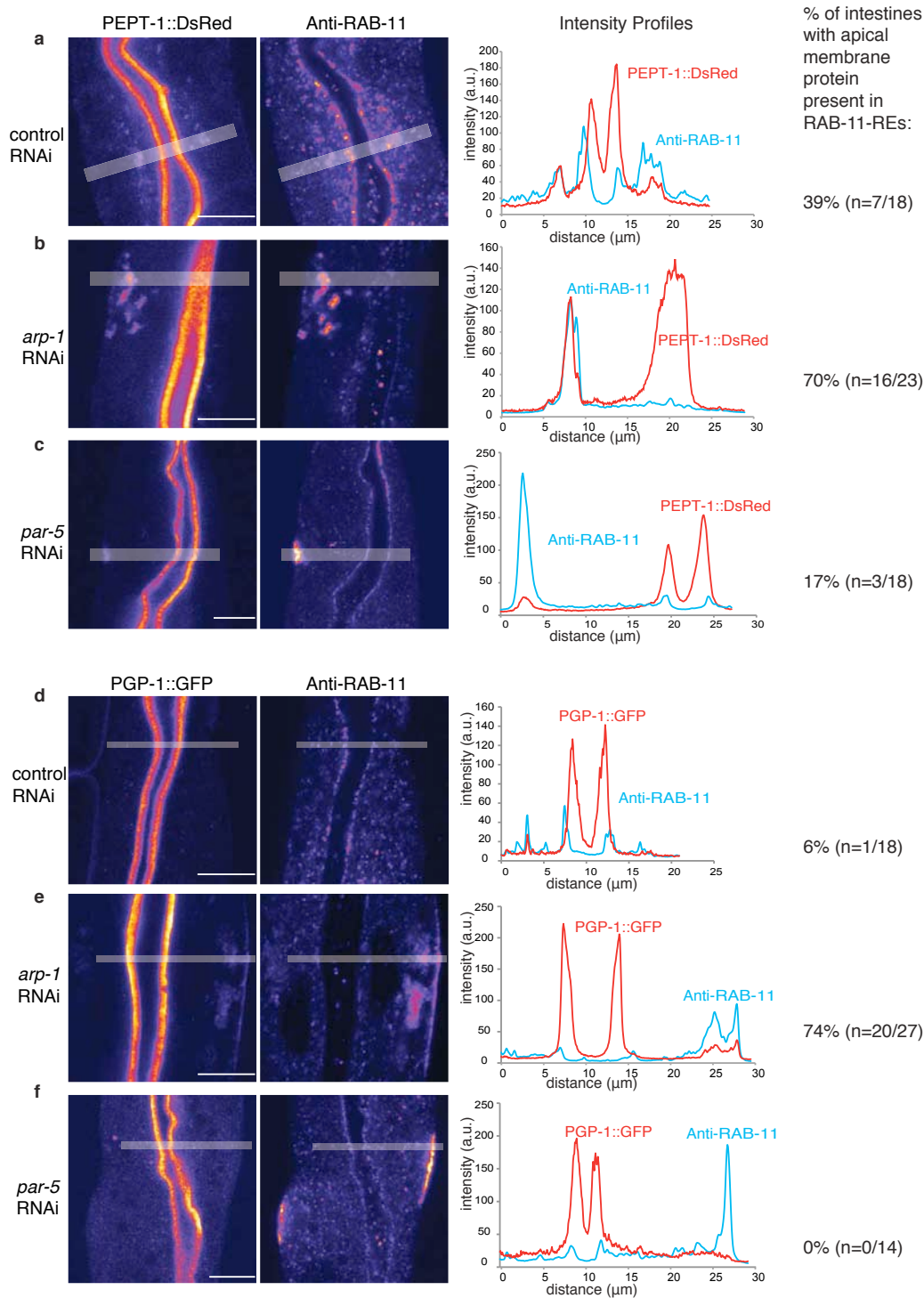


Figure S5 Apical membrane proteins PEPT-1::DsRed and PGP-1::GFP accumulate in basally mislocalised RAB-11-REs upon depletion of the dynactin-component ARP-1, but only weakly upon depletion of PAR-5. Line-based intensity measures (left: indicated by transparent lines on images, right: corresponding intensity profiles) on confocal images across intestines of worms expressing PEPT-1::DsRed (a-c) and PGP-1::GFP (d-f) immunostained for endogenous RAB-11. (a,d) In control RNAi intestines, PEPT-1::DsRed and PGP-1::GFP reside predominantly in the apical membrane, but small amounts are also present in RAB-11-labelled REs (in 39% (n=7/18) and 6% (n=1/18) of control RNAi intestines, respectively).

(b,e) Upon depletion of ARP-1, minus-end directed endosome transport is perturbed. Peripherally displaced RAB-11-REs contain significantly more apical membrane proteins PEPT-1::DsRed or PGP-1::GFP than REs in control conditions (in 70% (n=16/23) and 74% (n=20/27) of intestines with *arp-1* RNAi phenotype). Note that relatively more PEPT-1::DsRed than PGP-1::GFP accumulates in peripheral REs. (c,f) Compared to *arp-1* RNAi, depletion of PAR-5 causes little (PEPT-1::DsRed) to no (PGP-1::GFP) accumulation of apical membrane protein in peripherally clustered RAB-11-REs. For all samples, n derives from three independent experiments. Scale bars indicate 10μm.

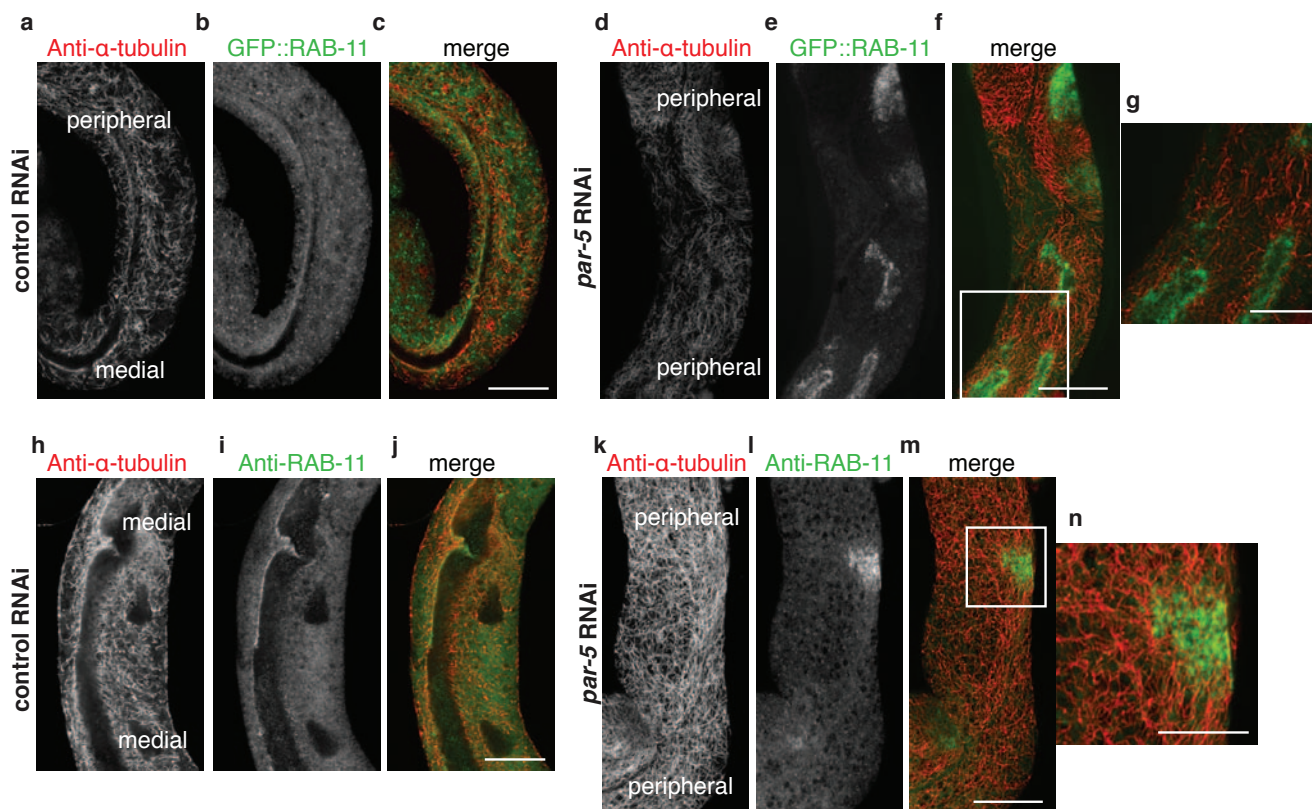


Figure S6 Microtubule cytoskeleton organisation is subtly altered at sites of peripherally clustered REs in *par-5* RNAi treated intestines. (a-c) Control RNAi intestine imaged at both peripheral (top) and medial (bottom) planes. In control RNAi, GFP::RAB-11-labelled REs are not peripherally clustered at the basal domain. Microtubules are distributed throughout the cell. (d-g) In *par-5* RNAi,

the microtubule organisation proximal to peripherally clustered REs appears to be subtly changed, with microtubules orienting towards the clusters (g). (h-n) Similar changes were also observed in non-transgenic intestines (NL2099 strain), immunostained for α -tubulin and endogenous RAB-11 upon control (h-j) and *par-5* RNAi (k-n). Scale bars indicate 20 μ m, and in g and n 10 μ m.

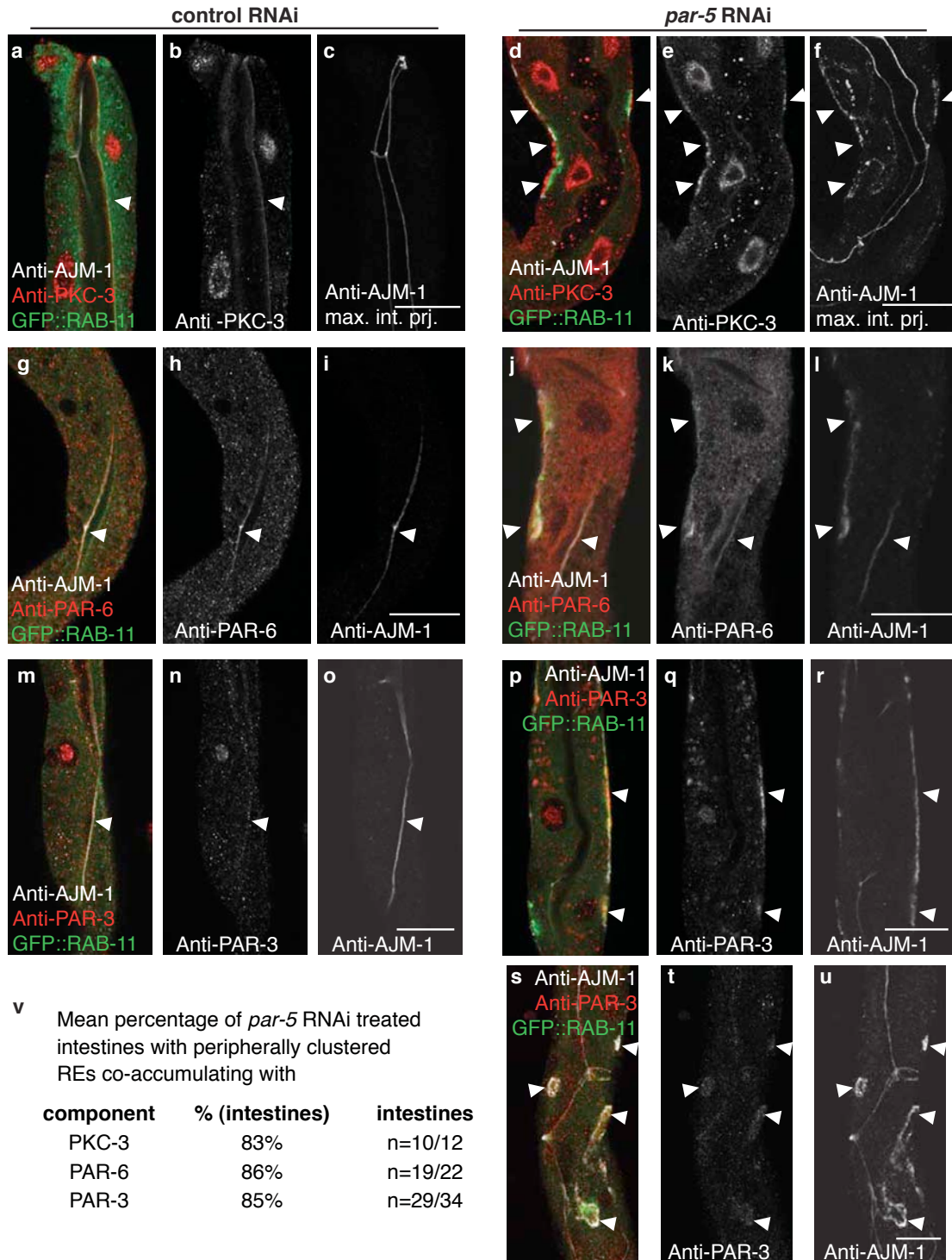


Figure S7 Ectopic localisation of apical PAR proteins at sites of clustered REs. (a to g”) Immunofluorescence stainings of GFP::RAB-11 expressing intestines. In control RNAi intestines, PKC-3 (b), PAR-6 (h), and PAR-3 (n) are more concentrated along the apical domain. PAR-6 and PAR-3 localise to AJM-1 labelled apical junctions. In PAR-5 depleted intestines, PKC-3 (e), PAR-6 (k), and PAR-3 (q,t) accumulate at ectopic, cortical sites positive for AJM-1 and peripherally clustered REs (see arrowheads). Although immunofluorescence signals of the endogenous proteins could

be weak, such as in the case of PAR-3 (n,q,t), the apical signals were sensitive to RNAi of *pkc-3*, *par-6*, or *par-3*, respectively. In phenotypic *par-5* RNAi enterocytes, the apical concentration of AJM-1, PKC-3, PAR-6 and PAR-3 can be reduced. (v) Mean percentage of *par-5* RNAi treated intestines with peripheral RE-clusters at which apical PAR-proteins co-accumulated ectopically. The number of analysed intestines n derives from up to four independent experiments. Scale bars indicate 20µm.

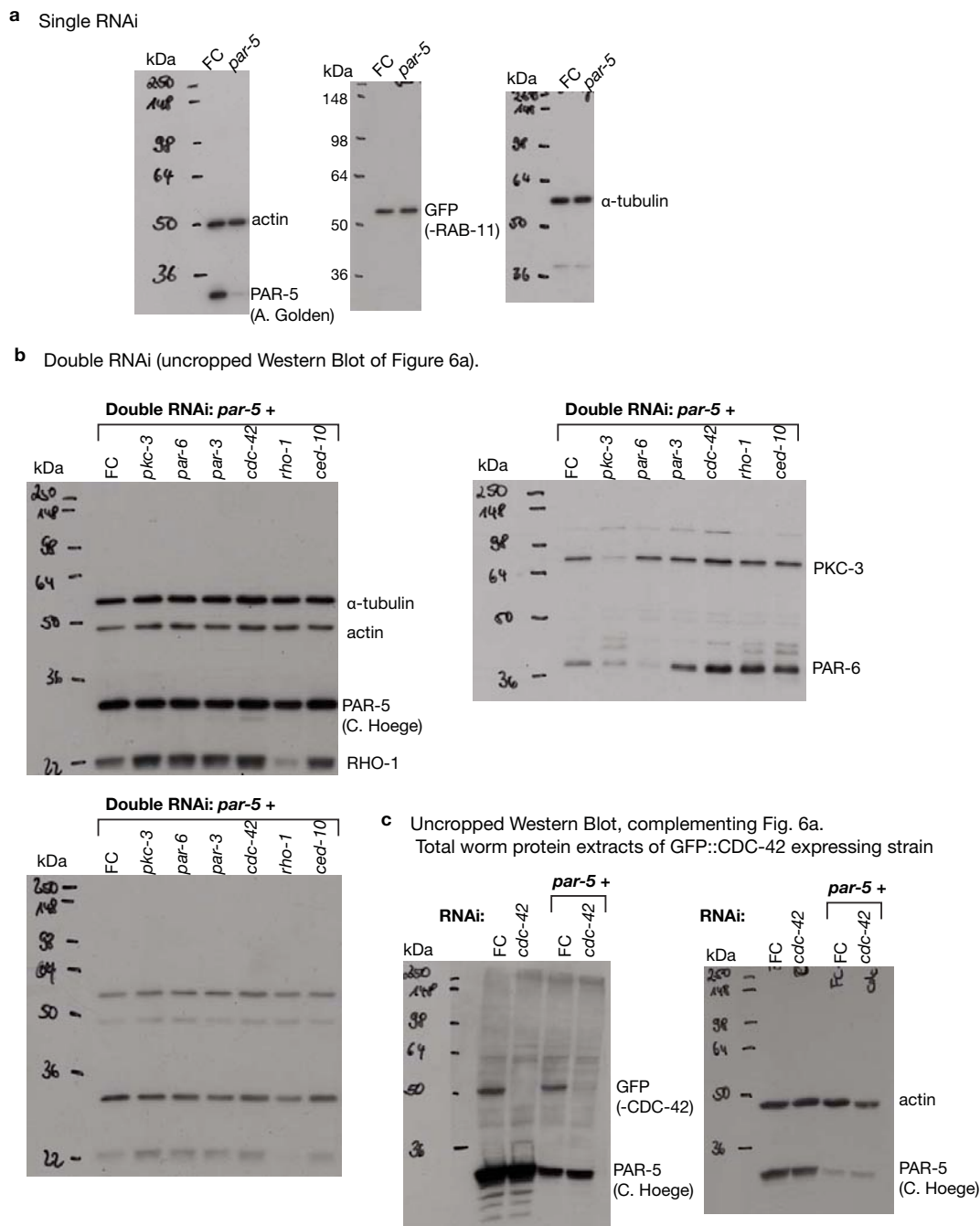


Figure S8 Full scans of Western blots. (a) Total worm protein extracts after treatment with single RNAi of feeding control (FC) versus *par-5*. Whereas PAR-5 is efficiently depleted, the probing for actin, GFP::RAB-11, and α -tubulin reveal no significant differences between control and *par-5* RNAi samples. (b) Full scans of Western blots cropped for Figure 6a. Total worm protein extracts after treatment with double RNAi of *par-5* + FC (the reference sample) versus double RNAi of *par-5* + an apical *par*-gene or a *rho* GTPase-gene (the test samples). The left two images show different exposures of the same immuno-probings (primary antibodies indicated at the right margin of the upper image). The right image shows one exposure of anti-PKC-3 and PAR-6 probing. Importantly, the total worm protein extracts of both reference and test samples have similar levels of PAR-5 depletion,

i.e. similar PAR-5/ α -tubulin or PAR-5/actin ratios. This shows that the suppression of the clustering phenotype in the test samples is real and not due to insufficient *par-5* RNAi. Efficient depletion of RHO-1, PKC-3, and PAR-6 is visualized in the appropriate double RNAi samples. Reduced PAR-6 levels upon *pkc-3* RNAi were observed in three independent experiments. *Ced-10* (*rac1*) RNAi is coupled to reduced GFP::RAB-11 intensities (not shown). Extracts in a and b were prepared from MZE98R worms. (c) Full scan of Western blot complementing the data shown in Figure 6a. Since no specific CDC-42 antibody was available, the efficacy of CDC-42 depletion in single and double *cdc-42* RNAi was confirmed by using total worm protein extracts of GFP::CDC-42 expressing strain treated with single RNAi (left two lanes) or double RNAi with *par-5* (right two lanes).

Supplementary Tables

Supplementary Table S1 Hit list of the primary HCS with a total of 356 hits and their phenotype profiles. Gene annotations comprise Wormbase descriptions (release WS 204), NCBI KOGs, Protein ID of the highest metazoan orthologue, InterPro domains (v.22.0), HMMerThread domains, OMIM disease information, sequencing results, as well as secondary assay results for 60 genes. For 92 of the genes in common with the *rme*-screen of Balklava et al. 2007, we included the published information on *rme*, *sec*, or both phenotypes. The second worksheet lists the 14 phenotypic defect categories and provides more detailed descriptions of these.

Supplementary Table S2 Identified protein complexes with established regulatory roles in membrane trafficking exhibit characteristic RNAi phenotype profiles.

Supplementary Table S3 Phenotypic and functional profiling of secondary assay genes. Abbreviations: AF=autofluorescence, REs=apical recycling endosomes, EEs=early endosomes, ER= endoplasmic reticulum, LEs=late endosomes, LROs=lysosome-related organelles. Note that candidates are assigned to a specific functional group based on the most pronounced RNAi-induced phenotypic changes, although their overall RNAi phenotype is often more complex. For secondary assay image examples see Figure 3. (*) Knockdown affects also LRO positioning, integrity, or sorting of AF material. (w) 'Worm only' means that there is no gene with more than 50% identity in sequence similarity in any non-worm species, whereas all other candidates are conserved up to humans (listed known or characterized orthologues acc. to WormBase (release WS227)).

Supplementary Note 1

Supplementary Note 1 provides information on all key methods applied in the primary RNAi high-content screen and for its analysis. These primary screen methods comprise:

1. Automated bacteria processing
2. Nematode processing
3. Automated imaging of worms
4. Software-based image analysis for phenotype identification and assignment of phenotype profiles
5. Determination of sequence hits
6. Functional annotation of candidates
7. Orthology Information
8. Detection of biological process terms overrepresented in the dataset
9. Hierarchical clustering